Geochemical Variation of Copper Sulphides Within the Carrapateena deposit, South Australia.

Thesis submitted in accordance with the requirements of the University of Adelaide for an Honours Degree in Geology/Geophysics

Callum Crespan

November 2021

DISTRIBUTION AND GEOCHEMICAL VARIATION OF COPPER SULPHIDES IN THE CARRAPATEENA DEPOSIT, SOUTH AUSTRALIA

ABSTRACT

Carrapateena is an Iron Oxide Copper-Gold (IOCG) deposit which is located on the eastern margin of the Gawler Craton, 100km southeast of Olympic Dam. Mineralisation at Carrapateena is restricted to a steeply plunging, pipe-like body of hematite and hematite-granite breccias termed the Carrapateena Breccia Complex (CBC). Primary Cu mineralisation within the CBC occurs in hematite-sericite-chlorite dominated breccias as chalcopyrite ($CuFeS_2$) and bornite ($Cu_5FeS_{4)}$ with some trace chalcocite (Cu_2S). Secondary covellite (CuS) and digenite (Cu_9S_5) is also observed in association with primary chalcopyrite and bornite. A geochemical Cu/S zonation pattern extends laterally outward with a transition from bornite → bornite/chalcopyrite → chalcopyrite → pyrite. The precipitation of main stage Cu mineralisation chalcopyrite is believed to of formed through interface-coupled dissolution-reprecipitation reaction (ICDR) and overgrowth of pre-existing pyrite and hematite. Bornite then undergoes similar reaction replacing the previous generation of chalcopyrite.

Utilising Scanning Electron Microscopy (SEM) and Laser Ablated Inductively Coupled Plasma Mass Spectrometry (LA-ICP-MS) analysis of 8 polished rock pucks collected from drillhole EG20CAR2038. Evidence of back reaction ICDR replacement through exsolution and annealing textures of chalcopyrite, covellite and digenite from bornite grains was found. In instances of bornite-digenite overgrowth, significant increases in abundance of Ag and Cu were discovered at depths of 1150m. Exsolution of chalcopyrite from bornite at shallower depths of 878m ,923m, 966m and 1099m resulted in no increase of Ag, Ni, Co and an overall decrease in Cu from the original bornite grains. This study shows that during the cooling stages (150-250ºC) of Carrapateena's development significant movement of trace elements and major elements amongst Cu sulphides occurred via the interaction of low temperature, basic pH fluids resulting in enrichment at depth within the deposit.

KEYWORDS

Carrapateena, IOCG, Copper, Chalcopyrite, Bornite, Pyrite, Digenite, Silver, Cobalt, Bismuth

List of Figures and Tables

1. INTRODUCTION

The Carrapateena Iron Oxide Copper-Gold (IOCG) deposit was discovered in 2005 and is located 100km southeast of the Olympic Dam deposit (Sawyer, 2014). IOCG deposits are typically defined as having significant economic Cu and Au as the primary economic metals associated with hydrothermal ore styles and strong structural control. However, there exists significant conjecture concerning classification of IOCG complexes as too broad a term for similar deposits including skarn-like and carbonatite hosted deposits (Groves et al, 2010). The IOCG term within this paper will strictly refer to the most commonly agreed upon IOCG sensu stricto deposits. These deposits contain abundant Fe oxides (>20%) in the form of magnetite and/or hematite which confines the ore (Shaofeng, L & Shuixing, F, 2016). IOCG's can be intimately linked with igneous intrusions, and are generally temporally associated with large batholithic complexes such as in the case of Carrapateena with the Hiltaba suite and Gawler Range Volcanics (Williams et al, 2015., Shaofeng, L & Shuixing, F, 2016)

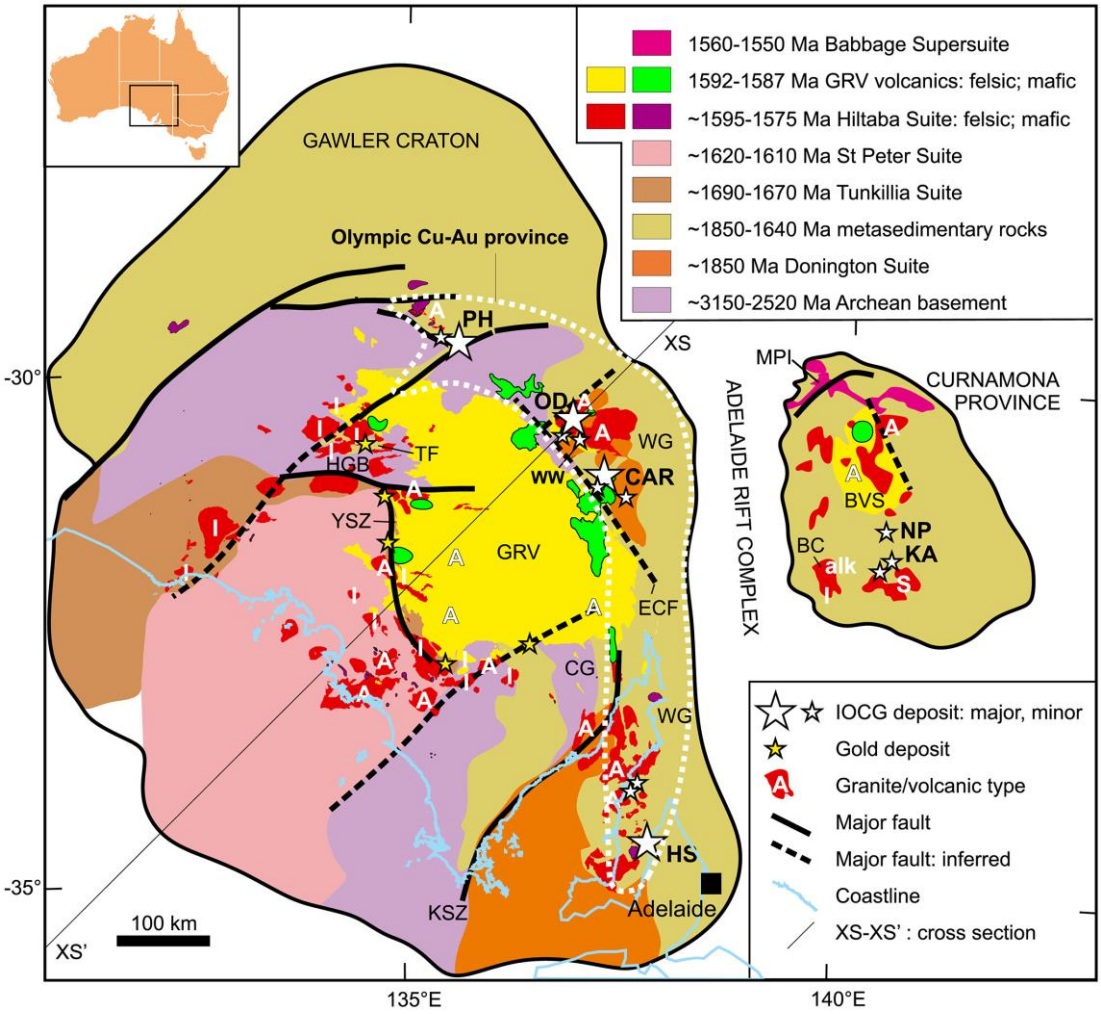

Figure 1: Figure exhibiting the interpreted regional geology of the Archean to early Mesoproterozoic Gawler Craton and Curnamona Province, showing locations of IOCG and Au deposits as well as granite and volcanic petrogenetic types (A, I, and S). (Skirrow et al, 2018) with input from Budd, 2006 Hand et al. 2007 and Cowley, 2008. Abbreviations: BC, Billeroo Complex; CAR, Carrapateena deposit; CG, Cooyerdoo Granite; ECF, Elizabeth Creek Fault; GRV, Gawler Range Volcanics; HGB, Harris Greenstone Belt; HS, Hillside deposit; KA, Kalkaroo deposit; KSZ, Kalinjala Shear Zone; MPI, Mt Painter Inlier; NP, North Portia deposit; OD, Olympic Dam deposit; PH, Prominent Hill deposit; TF, Tarcoola Formation; WG, Wallaroo Group; YSZ, Yarlbrinda Shear Zone.

Carrapateena has a Mineral Resource of 950 Mt at 0.57% Cu, 0.25 g/t Au and 2.7 g/t Ag (OZ minerals, 2020). Mineralisation occurs in hematite-sericite-silica-chlorite dominated breccias with primary Cu sulphide mineralisation present as chalcopyrite and bornite with trace chalcocite and secondary covellite and digenite. Chalcopyrite mineralisation is resultant of interface-coupled dissolution-reprecipitation (ICDR) and

overgrowth of pre-existing pyrite and hematite. High grade bornite then replaces chalcopyrite through similar reaction fronts as observed in other IOCG deposits such as Wallaroo (Sawyer, 2014., Porter, 2010., Neumann, 2019., Zhao et al, 2014., Kan Li et al, 2018). There are 3 main mineralisation zones present at Carrapateena with a central high grade bornite zone enveloped by a chalcopyrite and combined chalcopyrite/pyrite zone. (Sawyer, 2014., Neumann, 2019). This study utilises petrological and Scanning Electron Microscope (SEM) examination of samples from the designated bornite and chalcopyrite zones of the Carrapateena deposit to examine the paragenetic relationships and textures of Cu sulphides within these zones. Inductively coupled plasma mass spectrometers (ICP-MS) investigate the geochemical relationship between Cu sulphides and trace metals including Ag, Co and Bi. This project investigates Cu sulphide minerals to establish whether chalcopyrite and bornite precipitated from the same evolving hydrothermal fluid, or from differing temperature and pH environments.

2. GEOLOGICAL SETTING/BACKGROUND

2.1 Introduction to Iron-Oxide-Copper-Gold (IOCG) deposits

Carrapateena has been classified as hematite endmember of the Iron Oxide Copper-Gold deposits (IOCG) (Reid, 2019). These IOCG's are characterised by clear temporal and spatial relationship with large magmatic complexes composed of orogenic and/or subduction related granitoids and varying degrees of mafic phases (Williams et al, 2015., Skirrow et al, 2018., Schlegel et al, 2019). Global IOCG deposit ages range from the Neo-Archean to the Tertiary and correspond to significant periods of continental build up and extension, with the largest examples forming between ~1.65-1.45 Ga

(Skirrow et al, 2018., Reid, 2019), in South Australia's Eastern Gawler Craton. Examples include Olympic Dam, Prominent Hill and Carrapateena.

IOCG deposits have a characteristic style of host rock alteration with initial regional alteration comprising of relatively high temperature (400-600° C) Na-Ca alteration precipitating minerals such as albite, scapolite and magnetite (Hitzmann et al, 1992., Williams et al, 2015., Corriveau et al, 2019). Subsequent potassic alteration by fluids with more moderate temperatures (350-450° C) can then introduce significant amounts of Fe to the mineral system. This alteration is typically more structurally restricted and commonly includes its representative minerals such as biotite, K-feldspar, amphibole and magnetite. Deposition of economic ore minerals post-date these alteration stages and are believed to be the result of the interaction of multiple geochemically discrete hydrothermal fluids such as magmatic, basinal and/or metamorphic fluids (Gow et al, 1994., Hitzmann & Valenta, 2005., Williams et al, 2015., Schlegel et al, 2019). Continued lower temperature alteration leads to extensive overprinting hydrolytic alteration of sericite-chlorite and the formation of secondary Cu sulphides such as covellite and digenite with occasional exsolution and overgrowth of chalcopyrite from previous generation high temperature precipitated bornite. (Williams et al, 2015., Li et al, 2018., Corriveau et al, 2019).

IOCG's are broadly polymetallic, containing economic amounts of Cu, Au, trace metals (Co, Ag, Bi), rare earth elements (REE) and U (Hitzman et al, 1992., Reynolds L, 2000., Hitzmann & Valenta, 2005). Chalcopyrite and pyrite are the predominant sulphides present in IOCG's, however bornite and chalcocite can make a substantial percentage of the economic Cu grade of some deposits (Hitzman et al, 1992., Williams

et al, 2005., Barton, 2014). Au typically occurs as free grains or is enclosed within other sulphide minerals such as pyrite (Hitzman et al, 1992., Williams et al., 2005., Barton, 2014). U can be found within discrete minerals typically uraninite, brannerite and/or coffinite (Hitzmann & Valenta, 2005). REE have significant elevation in a number of IOCG deposits across the globe particularly Olympic Dam and Carrapateena with LREE preferentially incorporated into florencite, apatite and monazite and HREE within xenotime. (Jaireth, Hoatson & Miezitis, 2014., Barton, 2014., North, 2020).

Table 1: Common IOCG Cu sulphide species and their chemical makeup.

Important IOCG Sulphide Species	**Formula**
Chalcopyrite	$CuFeS_2$
Bornite	Cu_5FeS_4
Covellite	CuS
Digenite	Cu_9S_5
Chalcocite	Cu_2S

2.2 Regional Geology and Tectnothermal history

The Olympic Dam Cu-Au province is an area of significant IOCG mineralisation that extends 700 km along the eastern margin of the Archean-Mesoproterozoic Gawler demarcated by the dotted white line within Figure 1 (Fanning et al, 1988., Verdugo-Ihl et al, 2017., Skirrow et al, 2018). The IOCG endowed region is composed of Paleoproterozoic crystalline basement of metasedimentary and variable volcanic rocks of the Wallaroo group (~1850-1640 Ma). This group is intruded by the Donington Suite granites (~1850 Ma) which have their origin prior to and during the proposed Cornian Orogeny (Hand et al, 2007, Sawyer et al, 2017., Skirrow et al, 2018., Reid, 2019). The

Carrapateena region of the Olympic IOCG province formed during the early Mesoproterozoic as a result of the melting of fertile, metasomatized sub-continental lithospheric mantle, arc-related magmas intruded forming the bimodal Gawler Range Volcanics and Hiltaba Suite granites (~1595-1575 Ma) (Hand et al, 2007., Reid, 2019., Tiddy & Giles, 2020). The Gawler Range Volcanics and Hiltaba Suite granites are associated with regional deformation and metamorphism related to the Kararan Orogeny, (Hand et al, 2007., Reid, 2019). The period between ~1595-1575 Ma is proposed as the origin of IOCG deposits within the Olympic Cu-Au province including Carrapateena, Prominent Hill, Olympic Dam and a number of other undeveloped deposits including Khamsin, Fremantle Doctor and Oak Dam (Reid, 2019., Clark & Ehrig, 2020). The eastern portion of the province is overlain by Meso-Neoproterozoic sediments of the Stuart Shelf of the greater Adelaide Superbasin which correspond to rift basins related to the breakup of the super-continent Rodinia (~820 Ma), (Reid, 2019., Lloyd et al, 2020).

2.4 Local Geology

Mineralisation at Carrapateena is restricted to a sub vertical, pipe-like body of hematite and hematite-granite breccias termed the Carrapateena Breccia Complex (CBC) which covers an area 800 by 600 metres (Sawyer, 2014., Neumann, 2019). The deposit is overlain unconformably with 470 metres of Neoproterozoic sedimentary units from the Wilpena and Umberatana Groups.

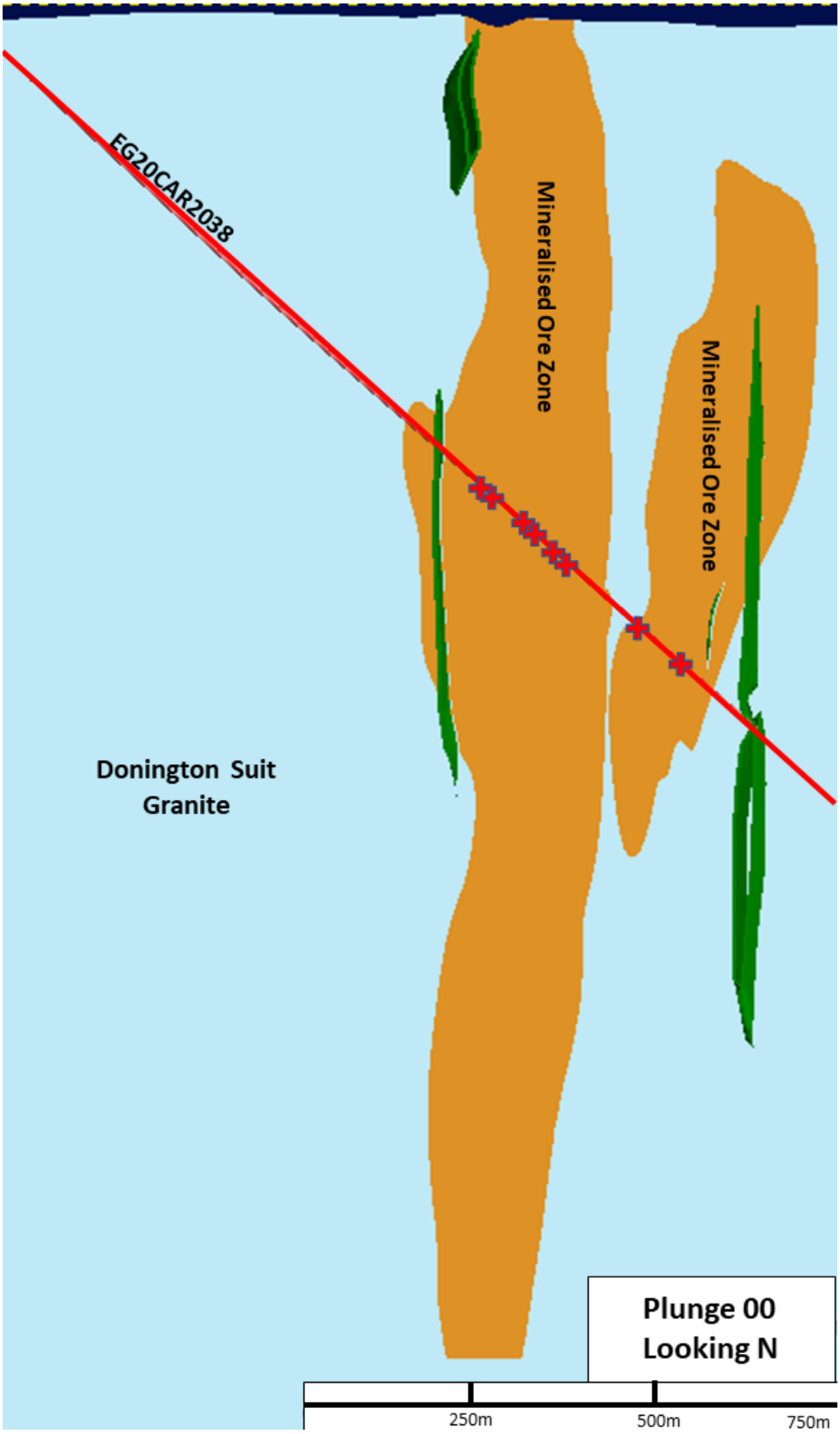

Figure 2: Model of the Carrapateena Breccia Complex orebody and the intersection of hole EG20CAR2038 looking to the north. Intervals sampled represented by crosses. Dykes within the deposit represented in green. (Model created in Leapfrog Gaehl, 2021).

The composition of breccias varies throughout the CBC, ranging from heterolithic clast hematite supported breccias to matrix-supported hematite breccias (Sawyer, 2014). Hematite is the dominant iron oxide present at the deposit with remnant magnetite present at typically at depth and as rare veins in the surrounding Donington granite (Sawyer, 2014., Neumann, 2019). Hematite has three main textures within the CBC ranging from red fine grained to massive grey through to coarse grey platy specular hematite (Vella & Emerson, 2009., Sawyer, 2014., Neumann, 2019). Hematite is the dominant alteration mineral within the CBC and its textures range from selective replacement of specific minerals to massive hematite within barren hematite zone on the northern margin of the CBC. The barren hematite zone is also deficient in Cu mineralisation can appear heavily leached and vuggy (Vella & Emerson, 2009., Williams, 2012., Taylor, 2014., Sawyer et al, 2017)

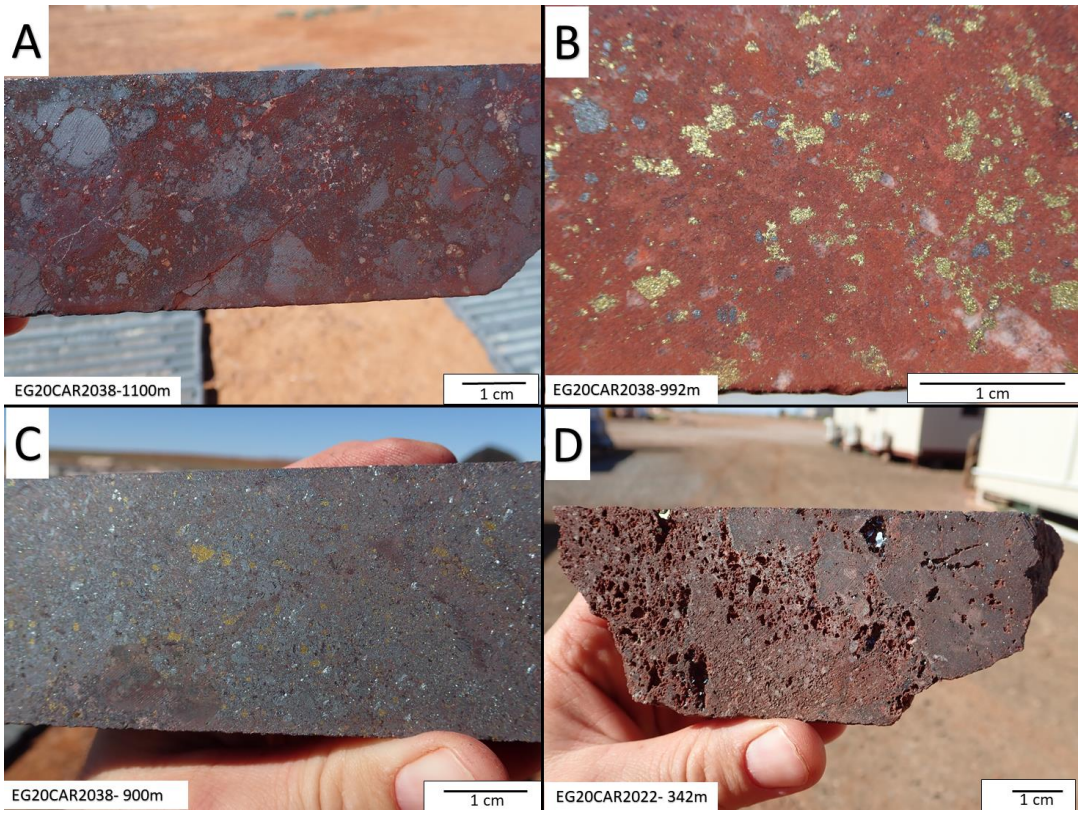

Figure 3: Visual representation of the 4 typical texture types present within the CBC: A) Coarse grey, clast hematite. B) Red fine-grained hematite with chalcopyrite mineralisation present. C)

Massive grey hematite with some chalcopyrite and bornite mineralisation present. D) Barren hematite zone showing vugginess with singular chalcopyrite crystal present in a vug (Photos by Richard Lily, 2021).

2.5 Mineralogy of Carrapateena

Primary Cu mineralisation within the CBC occurs in hematite-sericite-chlorite breccias as chalcopyrite, bornite with some trace chalcocite. Secondary covellite and digenite also occurred in association with other Cu sulphides. Cu shows geochemical Cu/S zonation pattern laterally outward from the CBC seen in Figure 2 with zones of: bornite → bornite/chalcopyrite → chalcopyrite → pyrite. The 3 main mineralised zones are composed of a central high grade bornite zone enveloped by the outer subsequent chalcopyrite and chalcopyrite/pyrite zones. Typically, within IOCG complexes mineralisation of main stage Cu chalcopyrite is formed through interface-coupled dissolution-reprecipitation mechanism (ICDR) and overgrowth of pre-existing pyrite and hematite. The breakdown of these pre-existing minerals provides adequate sulphur saturation for quick nucleation and precipitation of chalcopyrite grains when sufficient Cu is introduced to the system from various hydrothermal fluids into the system (Zhao et al, 2014., Li et al, 2018). Bornite replaces chalcopyrite similar to the replacement of pyrite and hematite as seen in Figure 4, once Cu saturation enables higher grade bornite precipitation typically at higher temperatures due to higher mobility of metal ions (Zhao et al, 2014., Li et al, 2018).

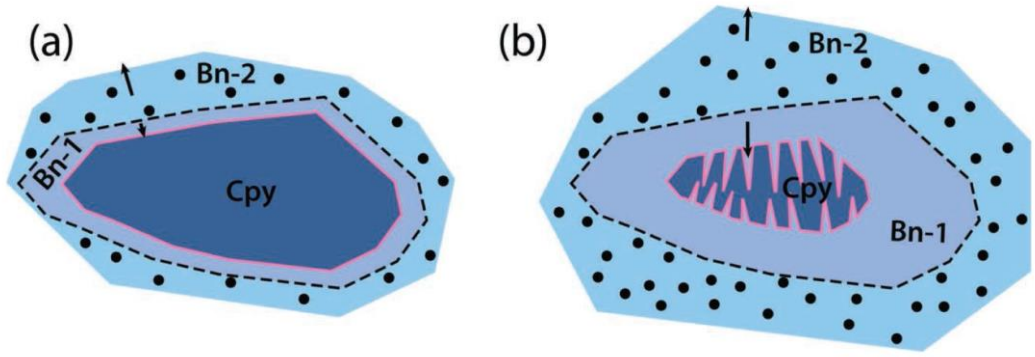

Figure 4: Example diagrams of ICDR reactions showing of partly reacted grain showing the reaction pathways in the replacement of chalcopyrite (Cpy) by bornite (Bn). The arrows signify the direction of bornite growth. Bn-1 forms via replacement of chalcopyrite, and Bn-2 via overgrowth. (a) Initially the reaction front progresses in a homogeneous manner within the chalcopyrite grain, but (b) the replacement then progresses mainly along cleavage planes of the chalcopyrite. (Zhao et al, 2014)

Similar instances of these reactions as well as exsolution of chalcopyrite and digenite from bornite are observed in this study as seen in Figures 5, 8, 9 and 11. Au and Ag are present as native grains and tellurides such as electrum, sylvanite and hessite as inclusions within Cu sulphides. The dominant U mineral present in the CBC is uraninite with minor brannerite and coffinite also found, with U mineralisation predominantly restricted to Cu-Au bearing hematite breccias (Sawyer, 2014., Kleeman, 2012). As with other IOCG deposits, REE are present at anomalous levels in the Carrapateena deposit (Sawyer, 2014., Fabris, 2020). Light REE are relatively more enriched then heavy REE and are typically found in the hematite rich breccias hosted in minerals such as xenotime and florencite (Kleeman, 2012., Sawyer,2014. North, 2020).

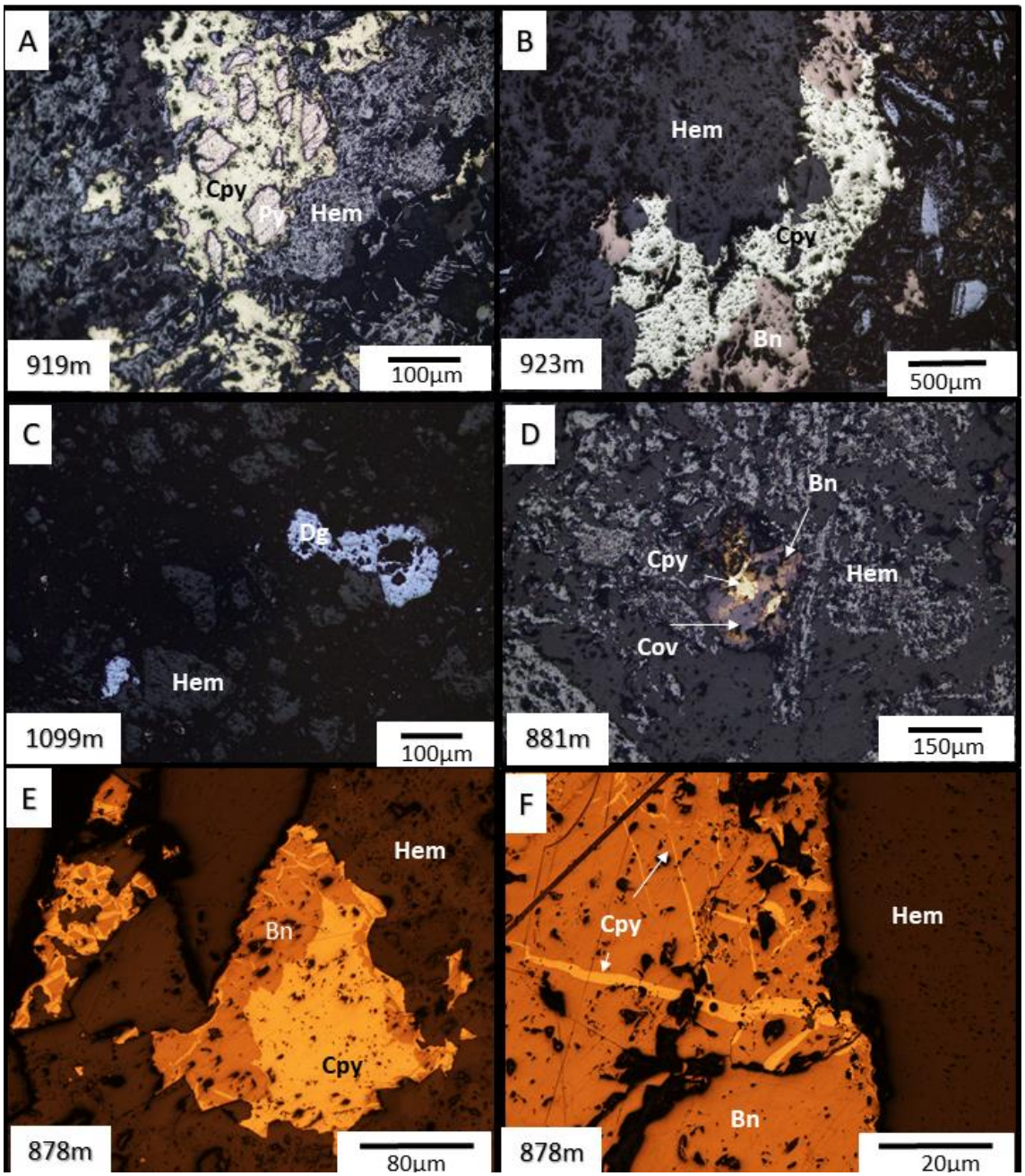

Figure 5: Examples of common sulphide species present within the CBC: A) pyrite inclusions hosted within chalcopyrite grains bounded by hematite matrix. B) intergrown bornite and chalcopyrite bounded by massive quartz and hematite. C) Digenite grains hosted within hematite matrix. D) Intergrown chalcopyrite-bornite-covellite grain within hematite matrix. E) Exsolution features of chalcopyrite from bornite. F) Exsolution lamellae chalcopyrite on boundary of bornite grain.

3. MATERIALS AND METHODS

3.1 Sample Collection and Preparation

Samples were collected from 3 diamond drill holes EG20CAR2038, RD20CAR2014 and RD20CAR2022 which intersect the CBC. Bornite and chalcopyrite zones were targeted based on Cu/S ratio with samples collected in areas of which the ratio exceeded 1.5 were deemed bornite zone. 8 samples of core were selected for further investigation to create an overview of sulphide and associated trace element mineralisation across the deposit (Figure 6). These 8 samples were divided into: 4 x bornite zone 1, 2x chalcopyrite zone, 1x bornite zone 2, and 1 of bornite zone 3 as seen in Figure 6.

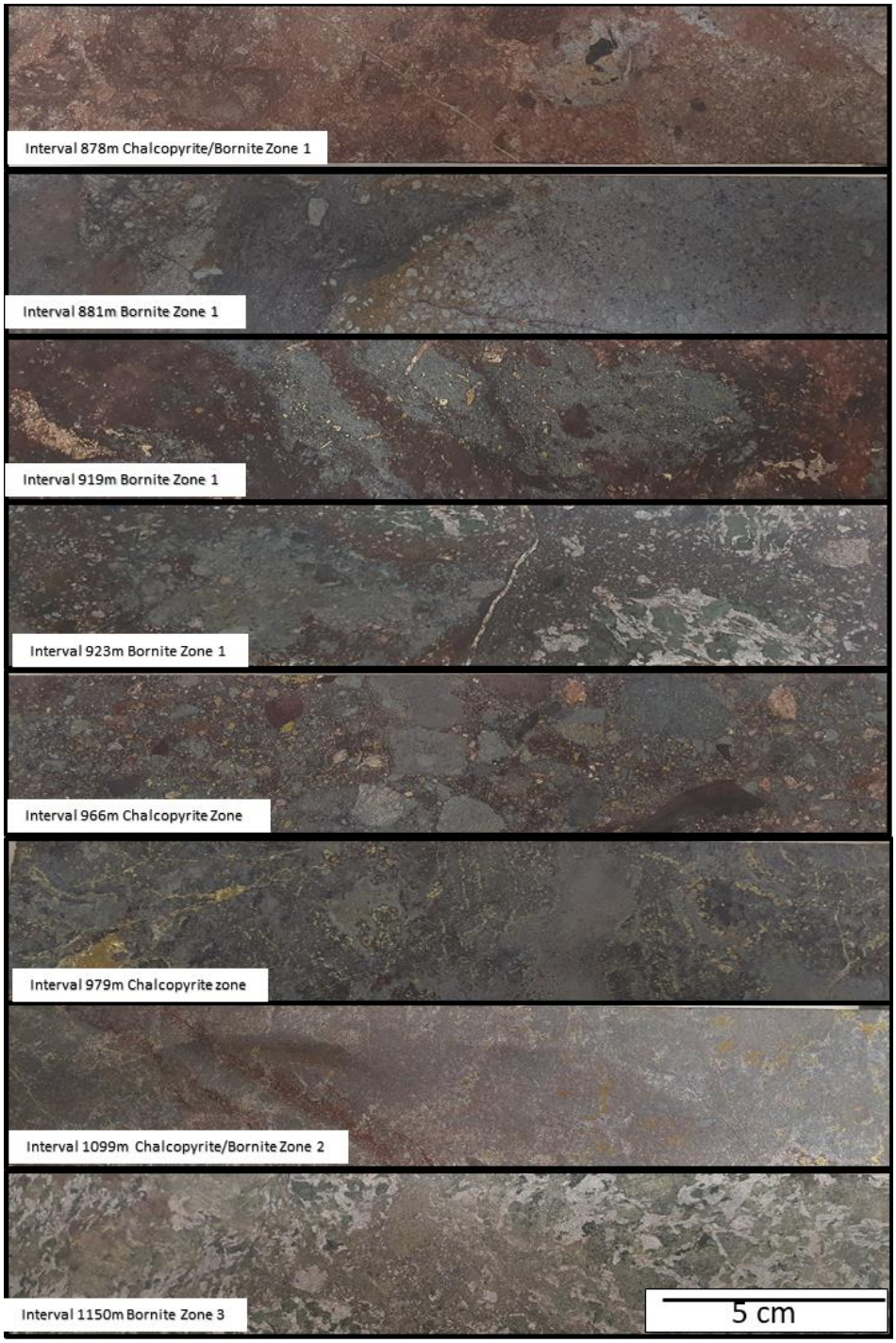

Figure 6: 8 core intervals selected for further analysis. Bornite zone 1 being the largest high-grade zone with variety of texture types from massive red hematite (878m, 919m) to predominant grey hematite (881m, 923m). Chalcopyrite zone separating bornite zones 1 and 2 predominantly clast supported grey hematite with replacement style mineralisation (966m) as well as massive grey hematite with major vein style mineralisation with replacement texture present also (979m). Bornite zone 2 massive grey hematite with replacement style chalcopyrite and bornite mineralisation. Bornite zone 3 heavily chloritized hematite almost entirely altered with solely bornite and some digenite mineralisation amongst chloritized hematite.

3.2 Optical Microscope

Each of the 14 pucks was observed under the Olympus BX51 System Microscope with a DP21 digital camera attached at Adelaide Microscopy, University of Adelaide. This was utilised to create familiarity with the samples and ascertain potential textures for further examination under the SEM with images taken of important textures.

3.3 Scanning Electron Microscope

The Hitachi 3800 SEM was utilised on 14 pucks created from the intervals seen in Figure 6 at Adelaide Microscopy, University of Adelaide. High resolution Electron Backscatter (EBS) images of individual mineral grains aided in analysis of textural relationships between minerals of interest, particularly sulphides, and their hosts to establish paragenetic timing. The X-ray energy dispersive detector (EDS) was used to ensure the correct identification of minerals through acquisition of qualitative elemental compositions. The technical settings for the Hitachi 3800 are listed in the Table 2.

Table 1:Technical settings for the Hitachi 3800 Scanning Electron Microscope.

Method	SEM3800
Samples	15
Spot Size	5
Beam Energy (Kv)	20.00
Working Distance (WD) (mm)	5

3.4 Laser Ablation Inductively Coupled Plasma Mass Spectrometry

Laser Ablation Inductively Coupled Plasma Mass Spectrometry (LA-ICP-MS) was utilised to obtain quantitative trace element data via the Agilent 7900x combined with the Resolution LR 193nm Excimer laser system at Adelaide Microscopy, University of Adelaide. Particular textures were selected to create geochemical maps of trace elements across different minerals. For this study, the laser ablation process used, a varying laser spot size of 8, 10 and 15 μm depending on size of each texture examined.

A scan speed of 40 seconds and a laser pulse rate of 10Hz was utilised. The raw data for each sample was processed using Iolite and Igor data processing software and compiled into elemental abundance maps. Each sample was integrated against chosen standards, STDGL3 (Danyushevsky L et al, 2011) and GSD-1G (USGS, 2011), and the background was removed. Elemental abundance was measured in counts per second (cps) with maps of textures created to visualise distribution. All samples were analysed for the following suite of elements: Ca^{43}, Al^{27}, Si^{29}, S^{34}, Fe^{57}, Co^{59}, Ni^{60}, Cu^{65}, Zn^{66}, As^{75}, Se^{77}, Ag^{109}, Cd^{111}, In^{113}, In^{115}, Sn^{118}, Sb^{118}, Te^{125}, Ce^{140}, Au^{197}, Hg^{201}, Ti^{205}, Pb^{206}, Pb^{207}, Pb^{208}, Bi^{209} and U^{238}. The maps were resized, re-processed for scale purposes and the cool to warm colour scale was used to identify the elemental trends most effectively.

3.5 Laser Spot Analysis

Laser spot analysis was also undertaken utilising the Agilent 7900x to determine the average definitive concentration of elements in PPM across samples. Spots were targeted on multiple minerals across samples such as pyrite, bornite, chalcopyrite and digenite to observe a complete picture of trace element abundance within each sample. Small intergrown textures were avoided for analysis due to threat of contamination from closely spaced ablation. Data was integrated against preselected standards: STDGL3 (Danyushevsky L et al, 2011) and GSD-1G (USGS, 2011) and processed through Iolite and Igor data processing software. All laser spots were analysed against the same suite of elements as LA-ICP-MS mapping as above with elements Co, Ni, Ag and Bi chosen for comparison. Refer to Appendix B for laser spot locations.

4. RESULTS

4.1 Bornite Zone 1 (Intervals 919 and 923)

Sample 919 SEM -MLA

The most common sulphide in this interval is chalcopyrite in the form of free clasts in a broadly hematite matrix as seen in Figures 7a, b, c. Chalcopyrite veining also crosscuts through hematite matrix and is strongly associated with quartz in these areas (Figure 7a-b). Some chalcopyrite clasts contain pyrite inclusions (Figure 7b-c). Pyrite was only identified as inclusions in 200-300µm chalcopyrite grains (Figure 7b, c). Chalcopyrite mineralisation is commonly related with the presence of quartz throughout the sample.

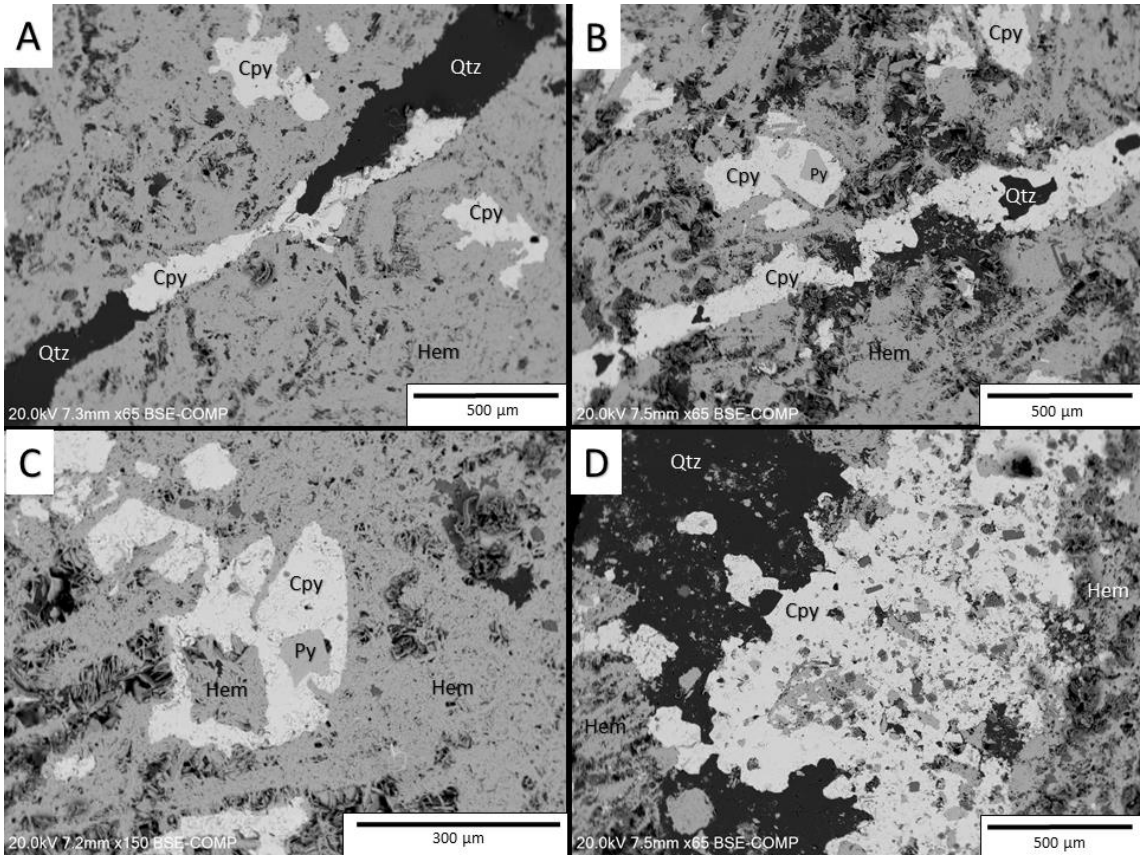

Figure 7: A) SEM image showing the two dominant textures in sample of chalcopyrite (Cpy) fragments within hematite (Hem) matrix as well as crosscutting vein style mineralisation with quartz (Qtz). B) SEM image showing contrast of veinlet chalcopyrite with hematite supported matrix chalcopyrite grains commonly with pyritic (Py) inclusions at their core. C) Common chalcopyrite texture of pyrite inclusions at core of grain. D) Large quartz grain in sample separated from hematite matrix by significant chalcopyrite mineralisation.

Interval 919 LA-ICP-MS

919 Texture 1: chalcopyrite-pyrite

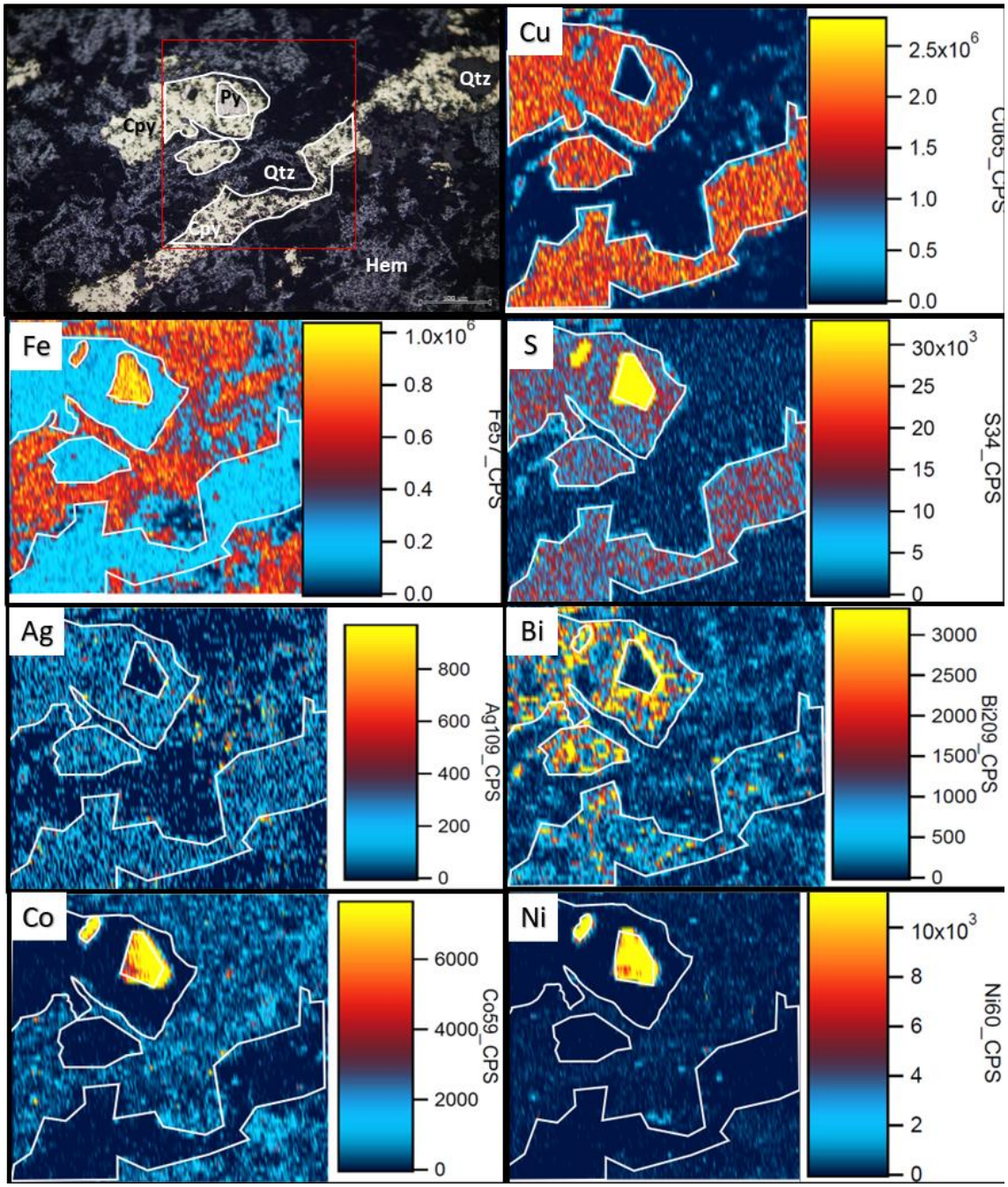

Figure 8: Photomicrograph showing the demarcated area of laser mapping of appointed texture with chalcopyrite (Cpy), hematite (Hem), quartz (Qtz) and pyrite (Py). Elemental maps of demarcated texture for: Cu, Fe, S, Ag, Bi, Co, Ni (Width of view 500µm)

The map displays that Cu remained elevated across both the veined chalcopyrite and clast with no noticeable difference in concentration. Pyrite has greater enrichment of iron than the surrounding platy hematite. Clast and veined chalcopyrite show no dissimilarities in abundance of Fe between them. Rims of chalcopyrite deficient in S compared to cores with pyrite heavily enriched in comparison. Ag enriched in chalcopyrite enough to demarcate boundaries of clasts and vein. Strong enrichment areas on rims of chalcopyrite and pyrite with some in hematite matrix. Pyrite exhibits deficiency in Ag. Bi has a higher abundance in the clast compared to the vein chalcopyrite, with the greatest abundance at the rims of the pyrite. The pyrite grains themselves are entirely deficient in Bi. Smaller clast of chalcopyrite below main clast, has no pyrite but still contains relatively enriched Bi. The chalcopyrite vein has patchy signals closest to the clast sulphide of Bi. Some zonation of Co is present within pyrite cores having a greater abundance. The hematite matrix has very minor enrichment of Co relative to chalcopyrite. Ni in this texture has a very similar relationship to cobalt only discernible by an even more depleted matrix of hematite and chalcopyrite.

Laser Spot Analysis Interval 919

Laser spot analysis was undertaken on sample interval 919 focussing around the texture shown in Figure 8. 3 spots were focussed on included pyrite grains with limited choice available due to size of pyrite inclusions. Another 5 spots were analysed across multiple chalcopyrite grains with 3 spots on grains with similar pyrite inclusions and 2 without (Appendix B).

Table 3: Laser spot analysis of pyrite and chalcopyrite from sample interval 923 with results of Co, Ni, Ag and Bi.

Spot number and mineral Targeted	Co Concentration (PPM)	Ni Concentration (PPM)	Ag Concentration (PPM)	Bi Concentration (PPM)
Pyrite 1	282	1944	7.6	46.2
Pyrite 2	227	1830	2.6	13.9
Pyrite 3	95.4	676	2.5	10.9
Chalcopyrite (Pyrite present) 1	0.27	0.3	7.01	25.4
Chalcopyrite (Pyrite present) 2	0.112	0.072	7.81	17.6
Chalcopyrite (Pyrite present) 3	0.26	0.07	7.8	22.7
Chalcopyrite 4	0.75	0.63	4.55	11.57
Chalcopyrite 5	0.82	0.66	4.39	2.3

Sample 923 SEM-MLA

The most common sulphide identified in this sample interval is bornite with minor chalcopyrite. Both sulphides share similarities with their textural appearance to that of preceding samples with some infill characteristics within hematite as well as appearing as inclusions within larger hematite grains. Bornite also appears as small inclusions or overgrowths within chalcopyrite clasts (figure 9a, b and c). The matrix is composed of intergrown quartz and varying degrees of chlorite alteration of hematite with some rare free native silver and electrum grains present. Silver tellurides and electrum grains also appear frequently within bn grains throughout sample (figure 9b and e). Figure 9d shows infill of bn within hematite grain core with remnant corona of hematite still present.

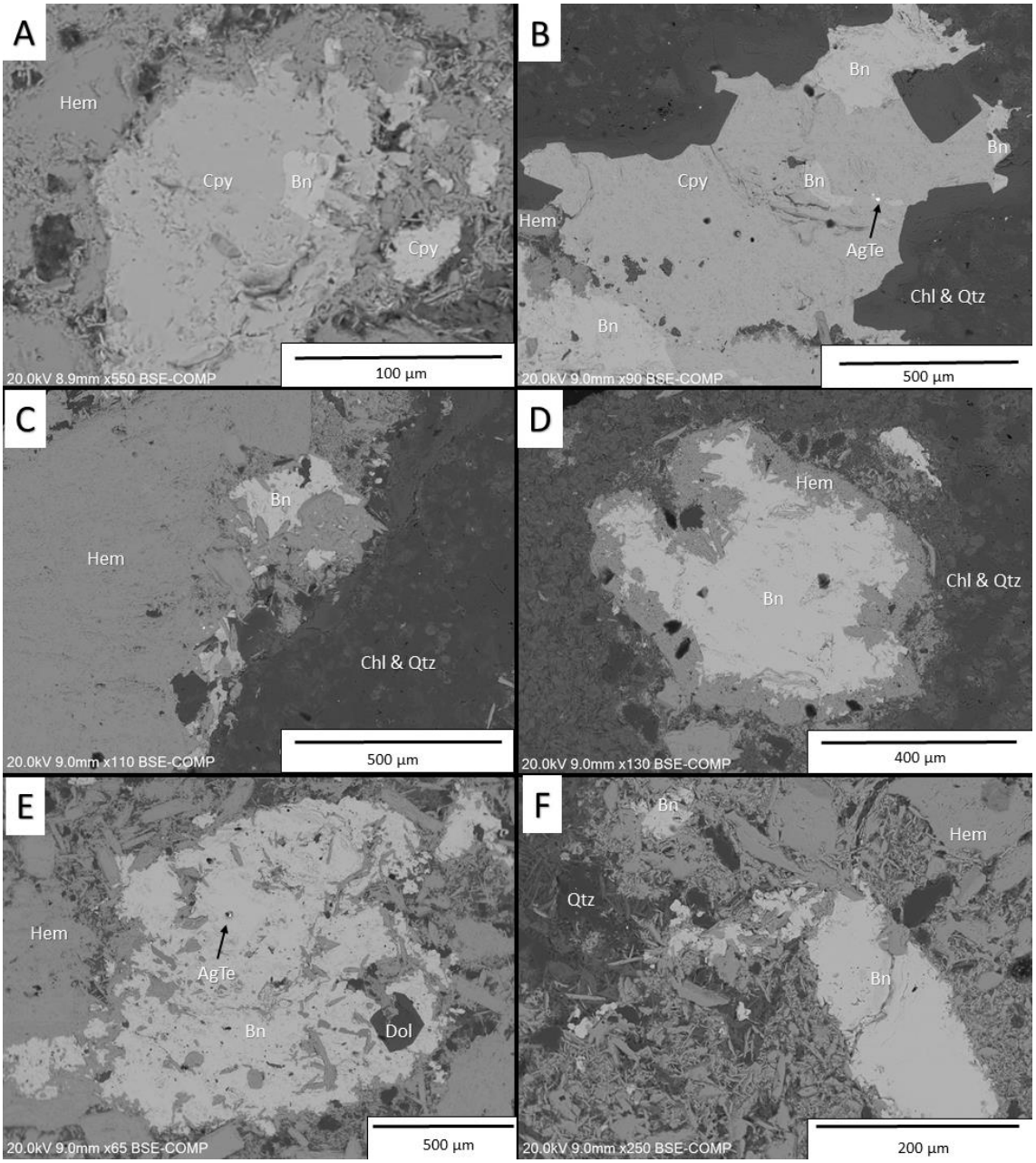

Figure 9: A) Chalcopyrite (Cpy) clast contained within hematite (Hem) grain with inclusions and overgrowths of bornite (Bn). B) Chalcopyrite grain in quartz/chlorite (Qtz, Chl) matrix with bornite inclusions as well as silver tellurides (AgTe). C) Bornite infill characteristics around hematite grains. D) Bornite grain with coronal assemblage of hematite around boundary of grain. E) Large bornite grain with dolomite (Dol), hematite and electrum inclusions. F) Intergrown bornite with bladey hematite.

Interval 923 LA-ICP-MS

923 Texture 1: bornite-hematite

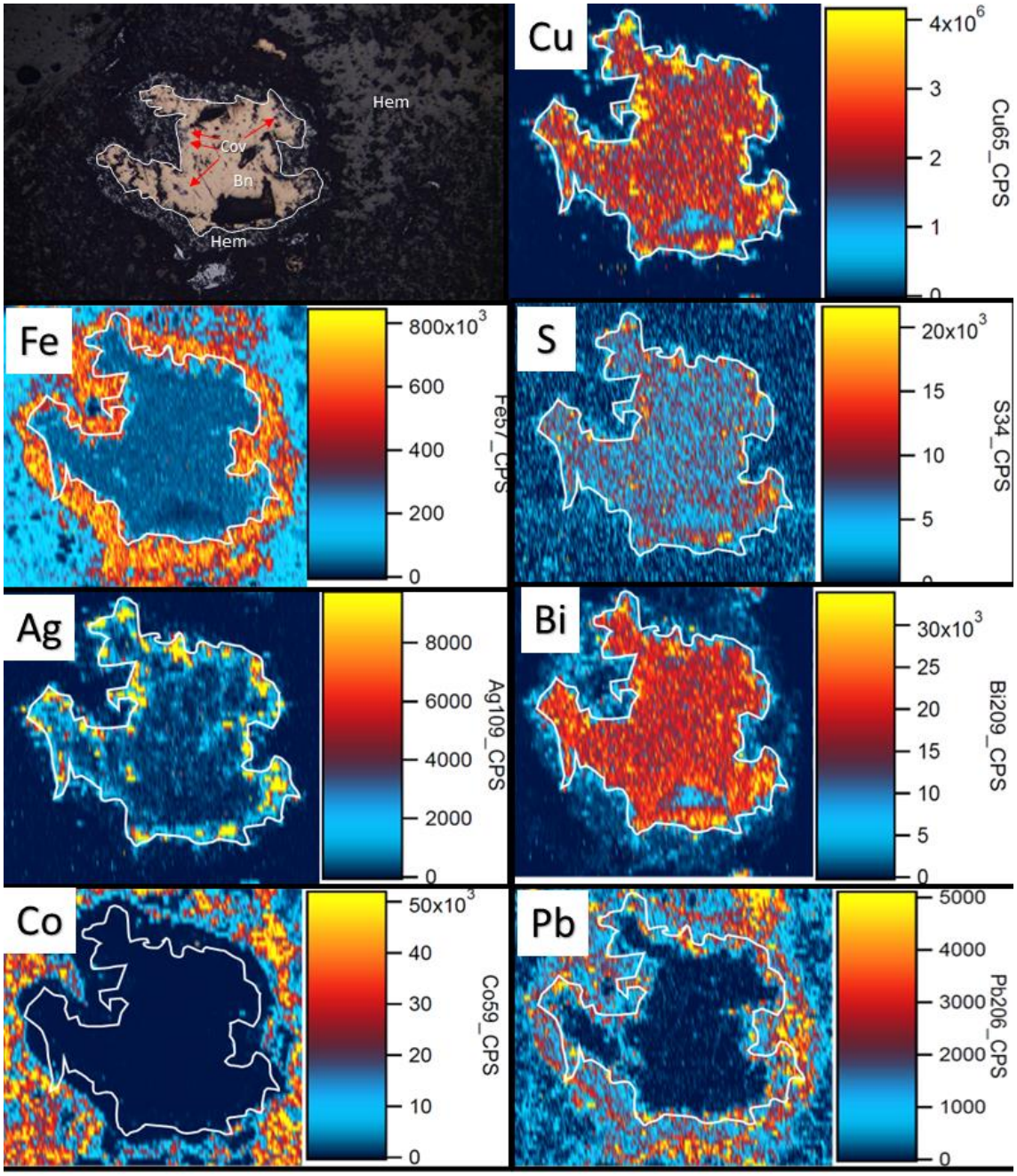

Figure 10: Bornite (Bn) clast with small covellite (Cov) overgrowths around rim that has a coronal hematite (Hem) assemblage around boundary of grain. Hole within bornite grain at bottom of grain Elemental maps of demarcated texture for: Cu, Fe, S, Ag, Bi, Pb, Co, Ni. (Width of view 700µm)

This texture shows high Cu concentration in anomalously large spots scattered around grain signifying areas of covellite. Fe depleted within core of bornite grain relative to rim. Elevated S and Ag spots confined to areas of covellite with rim of bornite elevated

in silver relative to core. Bi enriched in bornite grain with relative enrichment in rim found in similar areas to Ag, Co and Ni very elevated in the quartz matrix with none found in coronal assemblage or bornite grain. Pb shows patchy but highly elevated areas within the coronal assemblage of hematite.

923 Texture 2: bornite-chalcopyrite

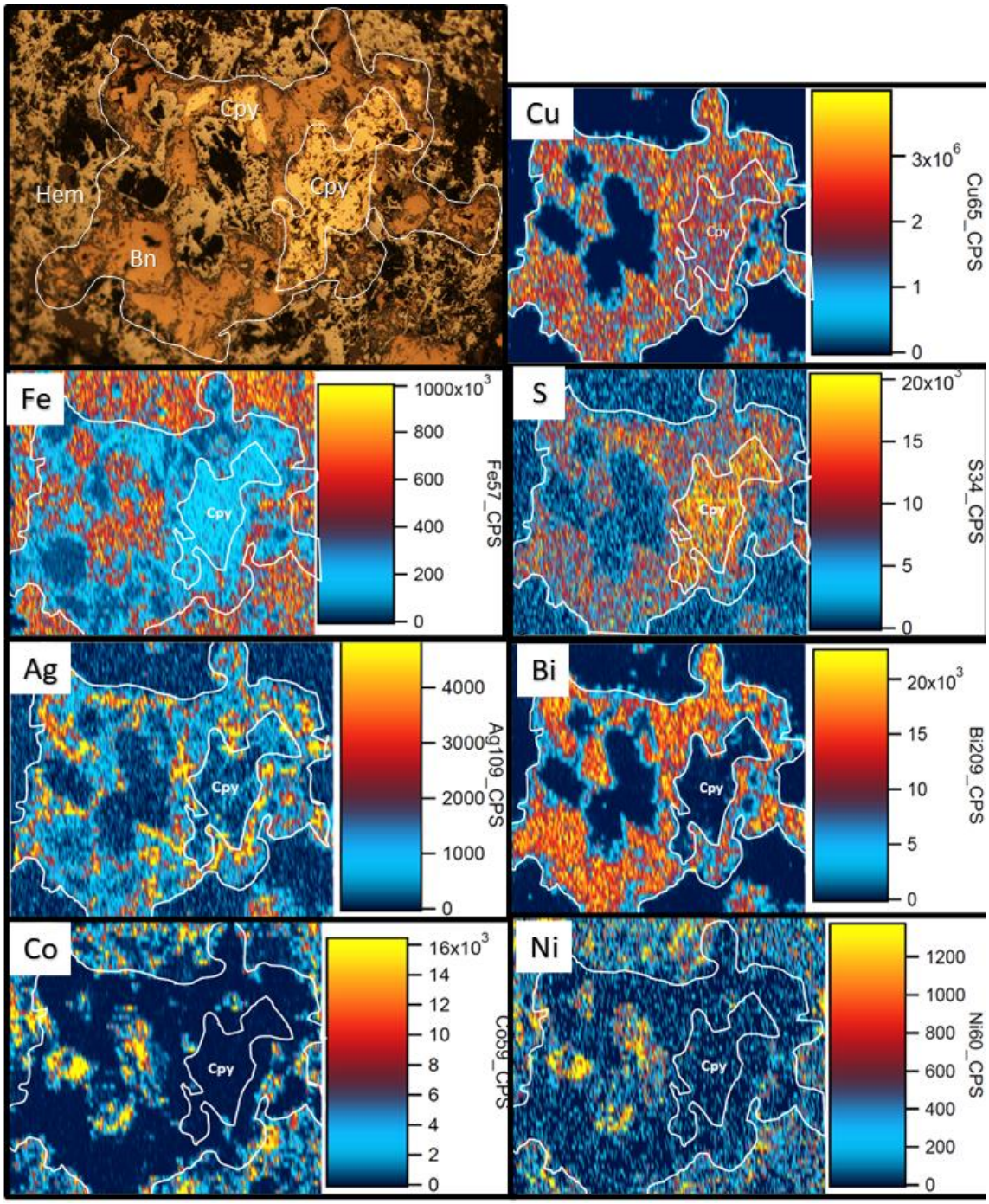

Figure 11: Chalcopyrite (Cpy) and bornite (Bn) grain intergrown within a matrix of hematite (Hem). Elemental maps of demarcated texture for: Cu, Fe, S, Ag, Bi, Co, Ni. (Width of view 700µm)

This texture shows Fe variation between the two copper species with noticeable elevated contents within the chalcopyrite portion. S contents also shows the differentiation between the species with chalcopyrite greater. Ag once again enriched in sections of bornite relative to chalcopyrite focussed along boundaries of grains. Bi highly abundant in bornite relative to chalcopyrite. Co and Ni both show greater abundance within hematite matrix and inclusions only. Sulphides depleted in these elements.

923 Texture 3: bornite-chalcopyrite

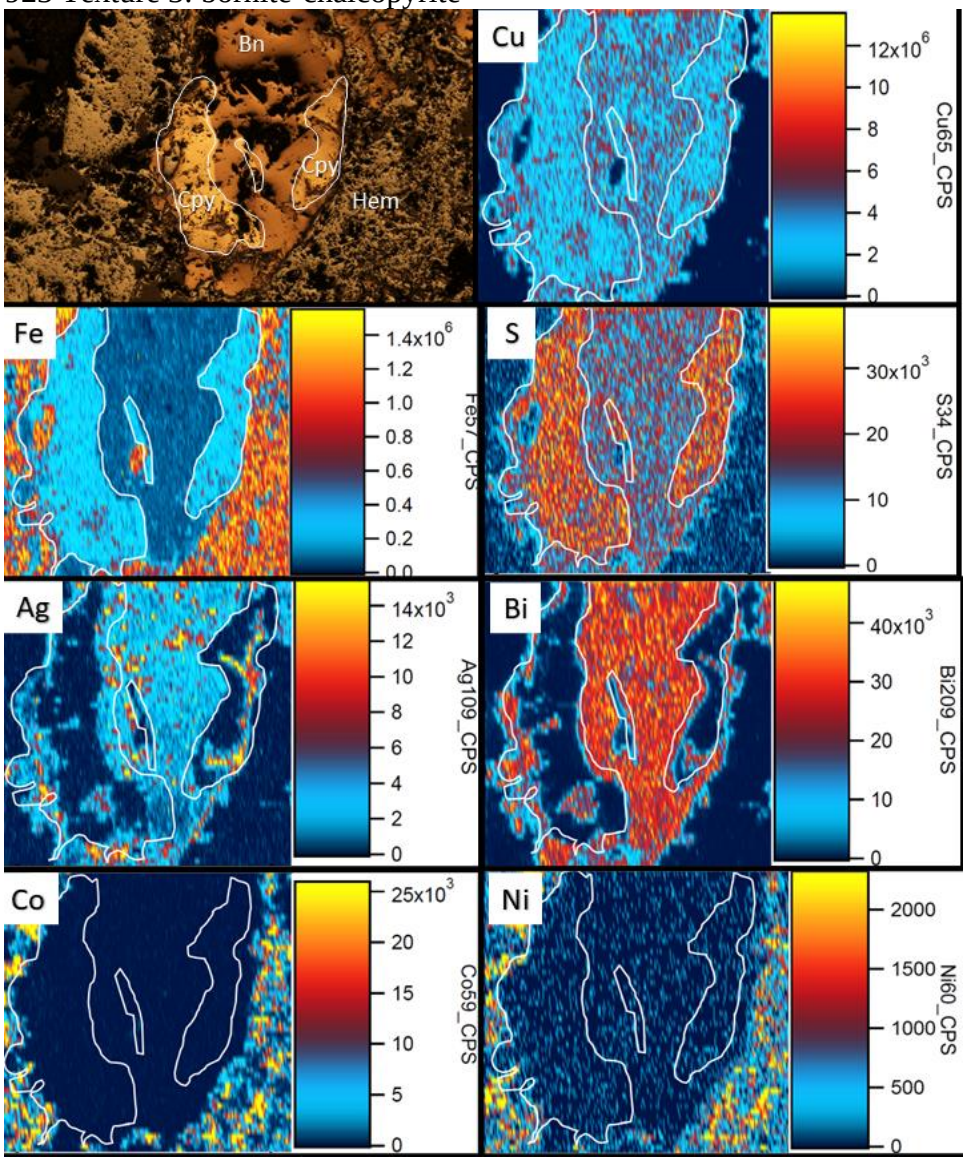

Figure 12: Intergrown bornite (Bn) and chalcopyrite (Cpy) within hematite (hem) matrix with nearby quartz (Qtz) clast. Elemental maps of demarcated texture for: Cu, Fe, S, Ag, Bi, Co, Ni, Pb (Width of view 500µm)

This texture shows the variation in the Cu rich bornite relative to chalcopyrite. Iron abundance also shows the distinction between the two species with the more relatively abundant Fe sections the chalcopyrite areas with the more minor abundance being that of bornite. Chalcopyrite is demarcated by high S, low Ag and Bi whilst bornite resembles the inverse. In particular high Ag and Bi can be seen in the right chalcopyrite grain along fractures which show bornite replacement. Ni and Co show relative high abundance within the hematite matrix.

4.2 Bornite/Chalcopyrite Zone 2 (Depth 1099m)

1099 SEM-MLA

SEM analysis of this sample interval identified bornite and chalcopyrite to appear coevally throughout this sample interval. Texturally chalcopyrite grains are the dominant sulphide with a significant vein running through the centre of sample. Large clasts of chalcopyrite were present with tendrils of bornite veins visible coming off boundary of these grains as seen in figure 13b. There are also examples of bornite and silver telluride inclusions within chalcopyrite clasts such as in figure 13a. In this sample chalcopyrite is strongly associated with areas of significant quartz mineralisation. Monazites in this sample are affiliated with copper sulphide mineralisation. Dissolution textures of monazite also appear in this sample as seen in figure 13c with inclusions of xenotime present. Rare bismuthinite grain observed on rim of monazite in close proximity to bornite grain (Figure 13d).

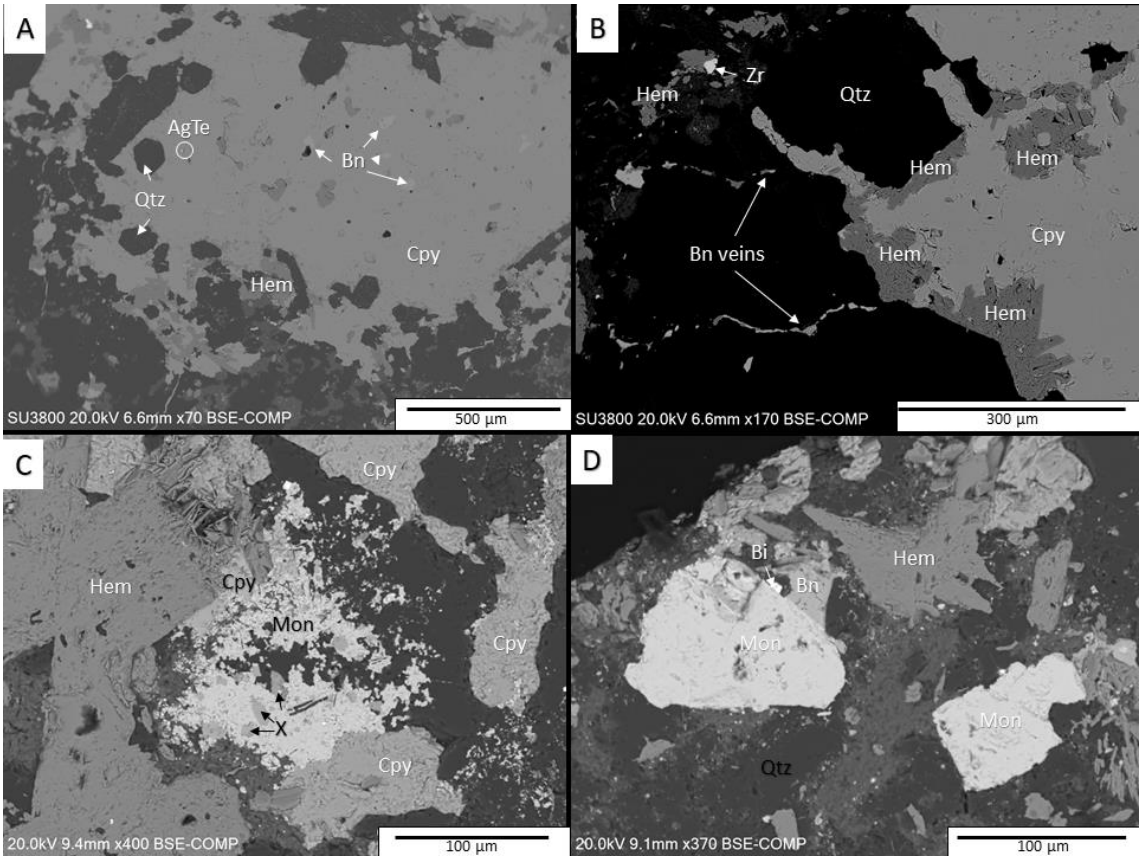

Figure 13: A) Section of dominant chalcopyrite (Cpy) vein in sample showing small inclusions of bornite (Bn) as well as euhedral quartz (Qtz) grains and some hematite (Hem). B) Another section of chalcopyrite vein exhibiting small veinlets of bornite trailing off main chalcopyrite clast with hm overgrowing rim, zircon (Zr) also present. C) Dissolution texture of monazite (Mon) with small visible xenotime (X) inclusions present. D) large monazite crystals in quartz matrix with small rare bismuthinite (Bi) grain present with nearby bornite.

Interval 1099 LA-ICP-MS

1099 Texture 1: chalcopyrite-bornite

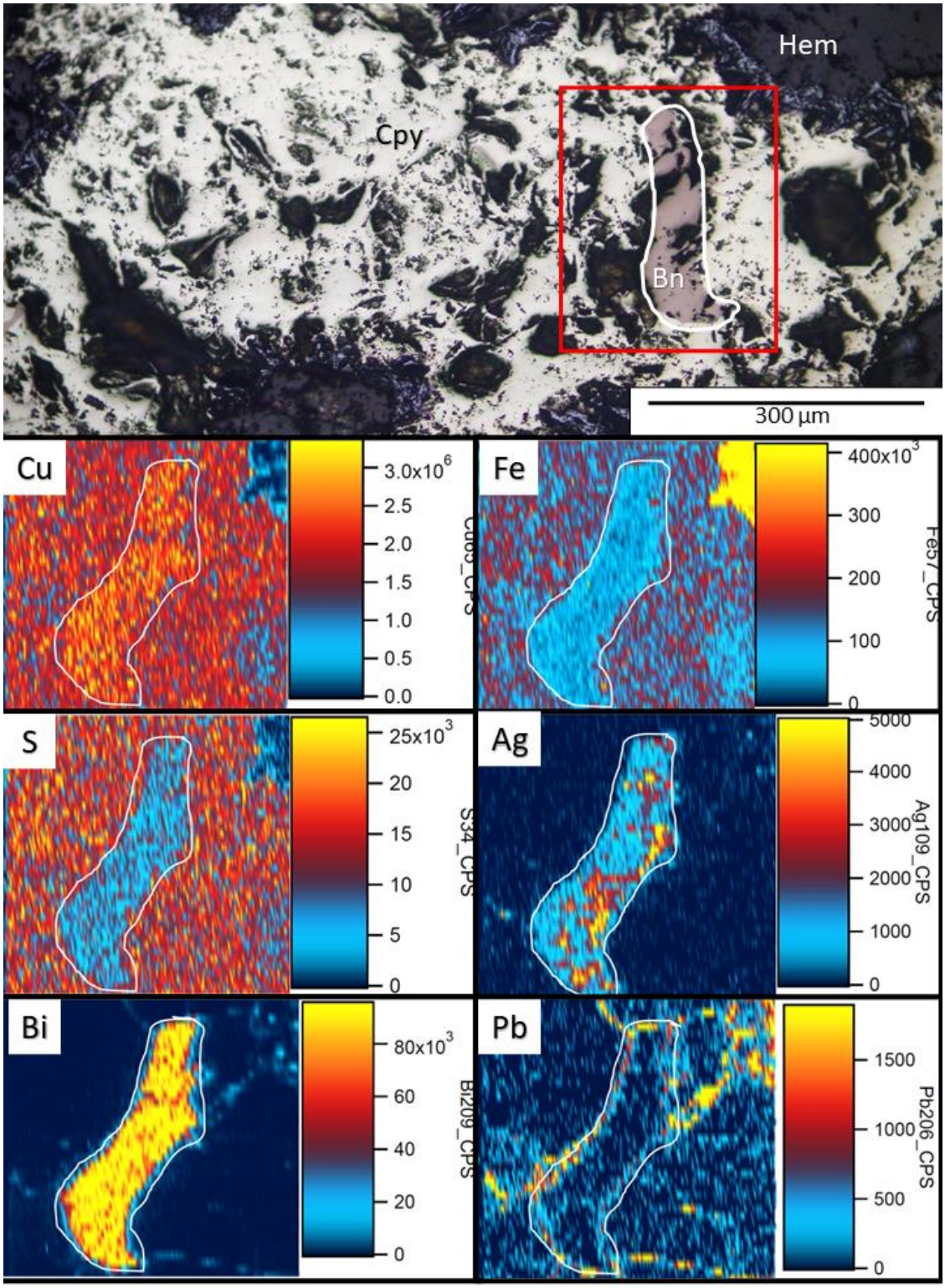

Figure 14: Portion of chalcopyrite (Cpy) vein bounded by hematite (Hem) matrix with inclusion of bornite (Bn). Elemental maps of demarcated texture for: Cu, Fe, S, Ag, Bi, Pb.

This texture shows Cu contents differentiation between the two sulphide species with the chalcopyrite vein enriched in Fe relative to the bornite inclusion with the variation of S clearly visible. Ag is enriched within the bornite inclusion particularly around the grain boundaries on the right side of the grain, chalcopyrite shows minimal to no abundance of Ag. Bi is highly focussed within the bornite inclusion with the grain rims depleted relative to core. There are small pathways of Bi enrichment that match with small veinlets of bornite. Pb is focussed around these small veinlets of bornite similar to Bi but mainly focussing around the boundary of the bornite grain.

1099 Texture 2: chalcopyrite-bornite-hematite

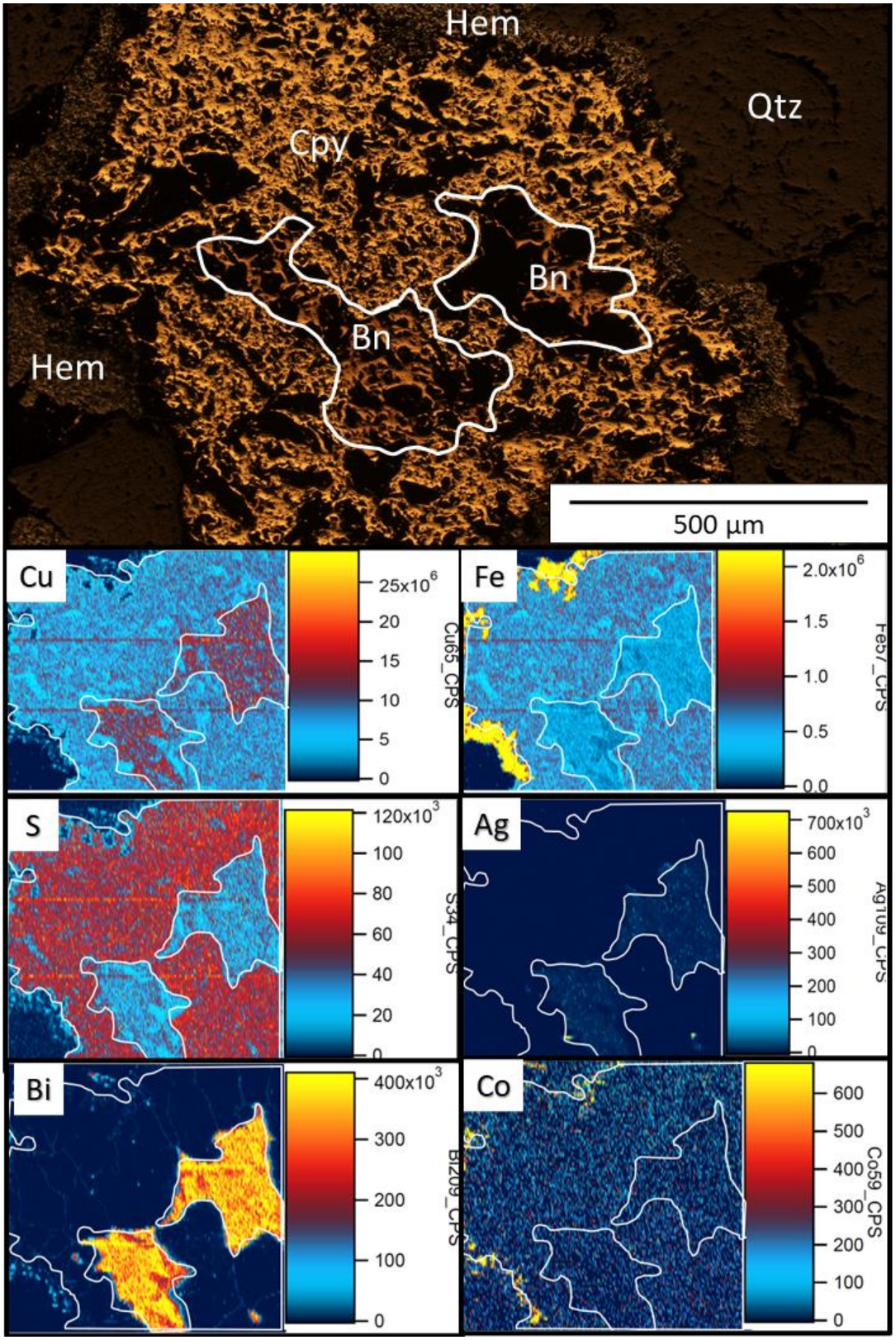

Figure 15: Bornite (Bn) inclusions encompassed by large chalcopyrite (Cpy) clast with a thin border of hematite (Hem) around periphery, texture hosted within a quartz (Qtz) matrix. Elemental maps of demarcated texture for: Cu, Fe, S, Ag, Bi and Co. (Width of view 1mm)

This texture shows elevated Cu abundance within the bornite inclusions relative to the greater chalcopyrite grain. Fe abundance is focussed in the hematite coronal boundary with some minor elevation in chalcopyrite. S is elevated within chalcopyrite with only minor abundance in bornite. Ag has a minimal abundance across the texture with small amounts restricted to the bornite. Bi is heavily abundant within the bornite relative to chalcopyrite with small veinlets coming off central bornite inclusions. Small abundances of Co are restricted to the hematite corona. Pb has small veinlets throughout the texture.

Laser Spot Analysis

Laser spot analysis was undertaken on sample interval 1099 with 6 spots sourced from multiple chalcopyrite grains across the sample. Another 6 spots were analysed across multiple bornite grains across the sample (Appendix B). Due to the intricate nature of intergrown bornite-chalcopyrite textures and to avoid contamination of signals from ablating two different minerals close together, only very large or standalone mineral grains were targeted.

Spot number and mineral Targeted	Co Concentration (PPM)	Ni Concentration (PPM)	Ag Concentration (PPM)	Bi Concentration (PPM)
Bornite 1	0.055	0.018	96.6	3388
Bornite 2	0.044	0.075	98.7	3159
Bornite 3	0.074	0.011	86.6	3250
Bornite 4	0.018	0.064	48.8	3231
Bornite 5	0.035	0.061	71.4	3168
Bornite 6	0.021	0.065	63.1	3252
Chalcopyrite 1	0.145	0.021	0.354	0.65
Chalcopyrite 2	0.181	Neg	0.571	1.33

Chalcopyrite 3	0.127	0.007	2	20.5
Chalcopyrite 4	0.169	0.032	2.48	4.43
Chalcopyrite 5	0.193	0	0.443	0.76
Chalcopyrite 6	0.166	0.021	0.299	0.72

Table 4: Laser spot analysis of bornite and chalcopyrite from sample interval 1099 with results of Co, Ni, Ag and Bi displayed in PPM. Neg= negligible readings below minimal threshold.

4.3 Bornite zone 3 (Depth 1150m)

1150 SEM-MLA

Sample interval 1150 has significant textural difference in comparison to previous samples including its mineralogical makeup and associations. Bornite is the most common sulphide present usually associated in and around quartz grains (Figure 16a, b). Silver tellurides are present as inclusions within bornite grains as seen in figure 16a. Matrix of this sample is heavily chloritized with multiple minerals showing dissolution and breakdown. Florencite is a relatively common mineral within this sample and is sometimes associated with bornite (figure 16c). Rutile also presents in this sample as well as zircon and monazites hosted within chloritic matrix (Figure 16e, f). Fluorite also present with one example seen in figure 16d fluorite infill cracks within bornite grain. Dissolution textures of monazite once again present with breakdown to xenotime (Figure 16f).

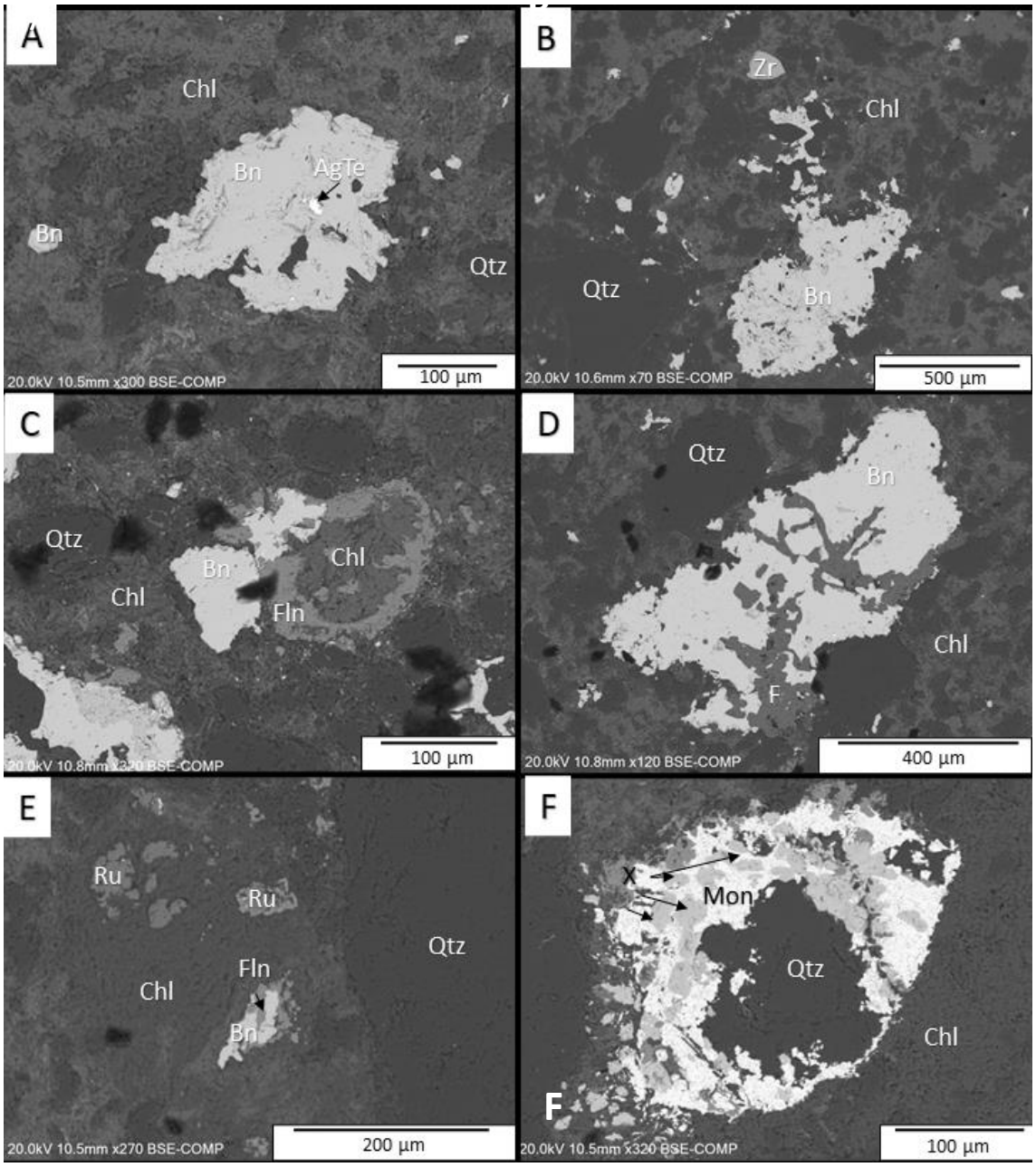

Figure 16: A) clast of bornite (Bn) hosted within chloritic matrix with significant inclusion of silver telluride (AgTe). B) bornite grain showing infiil around quartz (Qtz) clasts. C) Florencite (Fln) grain with chlorite (Chl) core and nearby bornite. D) Bornite grain infilled by fluorite (F) amongst internal cracks. E) Rutile (Ru) grains in chloritic matrix. F) Monazite (Mon) with xenotime (X) inclusions around quartz grain.

Interval 1150 LA-ICP-MS

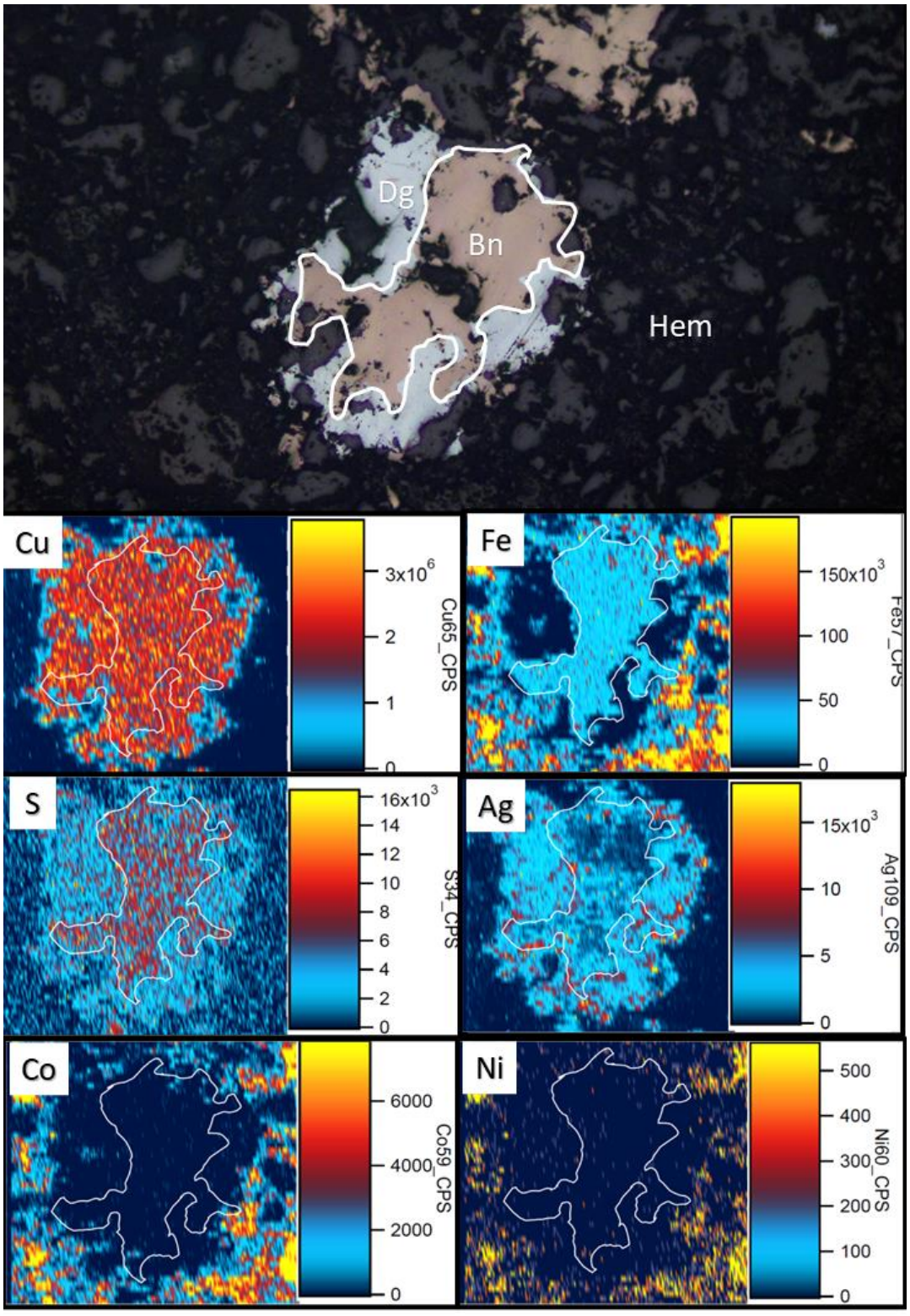

Figure 17: Intergrown texture of Bornite (Bn) and Digenite (Dig) within quartz (Qtz) matrix with demarcated area showing proposed laser scan. Elemental maps of demarcated texture for: Cu, Fe, S, Ag, Co, Ni (Width of view 400µm)

This texture shows the high abundance of copper across the bornite-digenite grain with no acknowledgeable difference in abundance across the two minerals. Iron within the bornite portion of the grain shows minor abundance relative to the heavily focused hematite matrix. The digenite portion of the texture shows minimal to no enrichment in Fe. S is enriched in the bornite portion with minor abundance across the digenite areas. Ag shows moderate abundance towards digenite areas of the grain over bornite with small areas of high abundance found along the boundaries of the two minerals. Cobalt is focussed within the matrix structure with little to no enrichment within the bornite-digenite grain.

Laser Spot Analysis interval 1150

Laser spot analysis was undertaken on sample interval 1150 with 5 spots sourced from multiple bornite grains across the sample. Another 5 spots were analysed across multiple digenite grains across the sample (Appendix B).

Table 5: Laser spot analysis of bornite and chalcopyrite from sample interval 1150 with results of Co, Ni, Ag and Bi displayed in PPM. Neg= negligible readings below minimal threshold.

Spot number and mineral Targeted	Co Concentration (PPM)	Ni Concentration (PPM)	Ag Concentration (PPM)	Bi Concentration (PPM)
Bornite 1	0.003	0.111	66.8	361.5
Bornite 2	0.002	0.007	66.1	341.8
Bornite 3	0.03	0.036	74.7	355.9
Bornite 4	0.001	0.052	95.2	369
Bornite 5	0.025	0.004	70	371.6
Digenite 1	0.156	0.052	310	7.2
Digenite 2	0.022	0.005	244.3	25.7
Digenite 3	Neg	Neg	263	7.8
Digenite 4	0.017	0.01	260.7	3.65
Digenite 5	Neg	Neg	264	4.33

DISCUSSION

Chalcopyrite

Chalcopyrite is the most abundant copper sulphide examined in drillhole EG20CAR2038. Paragenetically, chalcopyrite mineralisation has been hypothesised as a single prolonged event preceding or in conjunction with the precipitation of bornite in the early stages of the main Cu mineralisation (Sawyer, 2014., North, 2020), however textural analysis within this study has shown examples of chalcopyrite mineralisation which appears to postdate main stage mineralisation (Figures 5, 8, 11, 12 and 13). Initial chalcopyrite mineralisation within the hydrothermal conditions present within large IOCG style deposits such as Carrapateena occurs due to significant influx of free sulphur caused by the breakdown of pyrite and/or pyrrhotite and significant input of Cu

rich brines. Within the Gawler craton setting these Cu rich brines are generally attributed to either magmatic fluids associated with emplacement of the Hiltaba suite and Gawler range volcanics or metamorphic fluids released during regional deformation. (Skirrow et al, 2018., Reid, 2019., Schlegel et al 2019. Nucleation of chalcopyrite directly replaces pyrite/hematite from the pre-existing grain rim to the core as well as via overgrowth from the new chalcopyrite rim outwards (Figure 7 and 8) (Zhao et al, 2014). Multiple examples of replacement-overgrowth textures have been recognised from Carrapateena samples particularly chalcopyrite on pyrite textures found across sample intervals 923 (Figure 4 & 6) and 966. Exsolution features of chalcopyrite from bornite recognised in Li et al, 2018 can also be observed at Carrapateena shown in Figure 5 e and f through small lamellae of chalcopyrite visible in the broader bornite grains. The formation of these lamellae shows movement of Cu ions in the system even in the cool (<150ºC) temperatures associated with chalcopyrite exsolution.

Geochemically, chalcopyrite grains maintain a uniform trace element signature throughout the deposit with very little enrichment in elements measured such as Co, Ni and Bi. The biggest hindrance to the deportment of trace elements within chalcopyrite is the covalent structure of the chalcopyrite crystal lattice affecting the ability to host larger trace metal ions when other co-existing sulphides such as bornite are present (George et al, 2017). However, in chalcopyrite grains that contain pyrite inclusions seen in sample intervals 923 and 966, bismuth abundances are more elevated (25.4, 17.6, 22.7 ppm) relative to that of standalone chalcopyrite grains in other intervals (11.57 ppm, 2.3 ppm 919, 6 ppm 1099 and 0.17 ppm 878) (Figure 6). This enrichment may be indicative of the breakdown and replacement of pyrite which leaves bismuth with no

other compatible reservoir minerals available leading to higher-than-normal concentration within the usually deficient chalcopyrite (George et al, 2018). Whilst not as elevated in abundance as samples of pyrite-bismuth, silver maintains a very minor abundance with regularity across most samples of chalcopyrite observed with the highest being in pyrite hosting grains (6 ppm 919). Chalcopyrite shows some minor elevations in trace elements such as Ag and Bi across EG20CAR2038, however when present with bornite in exsolution like textures these elevations are not observed (Figures 14 and 15). This shows exchange of trace elements in the mineral system at low temperatures associated with exsolution of chalcopyrite. Similar exsolution textures observed at the Wallaroo IOCG deposit within Li et al 2018 are also seen in Carrapateena (Figure 5) indicating the nature of the exsolution products being driven by pH levels of small amounts of fluid present within the mineral structure (Zhao et al, 2017).

Bornite

Bornite has 3 distinctive zones examined in drillhole EG20CAR2038. The first zone initiates from 878m-932m with two smaller zones at 1094-1097m and 1155-1165m. However, bornite mineralisation is not restricted to these areas and can be found commonly throughout the hole in lesser abundance. Paragenetically, bornite is believed to postdate initial chalcopyrite mineralisation and forms due to ICDR and overgrowth of previous generation chalcopyrite as seen in Figures 5b, 9 and 11. It is believed this reaction is catalysed by 200-300ºC and neutral-basic pH hydrothermal fluids (Zhao et al, 2014). From SEM analysis, it was observed that bornite grains are common carriers for a multitude of tellurides particularly that of silver, gold and bismuth including

hessite, sylvanite and electrum with native metal inclusions also present within cracks and holes in the sulphide grains (Figure 9b, f and 16 a). On a geochemical level bornite is also a common host for “invisible” micron scale silver with comparatively high levels of abundance to that of chalcopyrite across the three bornite zones (average ppm: 74.56 ppm 1150, 77.53 ppm 1099 and 56.7 ppm 878). The Ag elevation across the bornite grains is relatively uniform throughout hole EG20CAR2038 although some hotspots of silver abundance in a bornite grain can be restricted to small overgrowths of covellite as seen in Figure 10. Without exception, levels of bismuth in bornite are elevated across the drill hole (average ppm: 86.8 ppm 1150, 359.96 ppm 878 and 3241 ppm 1099). This varying concentration across the different bornite zones may indicate multiple fluid interactions of varying temperature from 125ºC-250ºC associated with exsolution style textures and >250ºC temperatures during main stage synthesis (Zhao et al, 2017., Li et al, 2019). The case of micron scale silver and bismuth within bornite is not restricted to Carrapateena with examples of sulphide trace element reservoirs examined at Olympic Dam (Rollog et al, 2019., Cook et al, 2021). The partitioning of these metals into bornite and other copper sulphides may be due to the differences in crystal structure of each sulphide species. However, whilst at high temperatures bornite is found to be a strong reservoir of trace elements (Cook et al, 2021), as the precipitating fluids cool it is possible for these trace metals to exsolve and focus around pores and cracks within the grain leading to the formation of telluride and native metal inclusions as seen at Ann mason (Aird et al, 2021., Cook et al, 2021). This story of the shifting of metal endowment within these sulphide grains is shown by the multitude of telluride and native metal inclusions within Carrapateena bornite seen in Figure 9b, f and 16a.

Digenite

Digenite is another copper sulphide mineral observed within the Carrapateena sulphides and shares a complex solid solution relationship with bornite in the Cu-Fe-S ternary system (Zhao et al, 2017., Adegoke et al, 2021). It is typically the more enriched copper species with a formula of Cu_9S_5 although its Cu formulae varies across deposit systems (Zhao et al, 2017). Within hole EG20CAR2038, digenite is only observed at depth interval of 1150m in one of the smaller, deepest bornite zones. This depth interval is heavily chloritized and contains less than 20 small grains of digenite within the quartz-hematite matrix as well as one intergrown digenite-bornite clast. The intergrown clast texture shows the bornite regions of the grain restricted to the core of the grain whilst digenite is along the periphery. Under hydrothermal conditions within IOCG Cu-Fe-S systems digenite is hypothesised to be an exsolution product from bornite as hydrothermal conditions begin to cool below 160-210 degrees Celsius (Zhao et al, 2017., Adegoke et al, 2021). The composition of the Bn-Dg solid solution becomes richer in Cu with decreasing temperatures as well as Fe poor, thus providing ideal conditions for the preferential mineralisation of digenite (Zhao et al, 2014., Zhao et al, 2017). This texture (Figure 17) in conjunction with a low temperature formation supports a later stage paragenetic development of the digenite relative to the bornite and strongly mirrors exsolution and overgrowth of chalcopyrite from bornite. Geochemically, digenite shows a greater abundance of silver in comparison to that of bornite within the sample, with average concentrations of 268.4 ppm to bornite 74.6 ppm. These observations indicate during the annealing process and exsolution of digenite, exchange of trace elements such as silver, occur at depth in the deposit.

Examples of this phenomena are also present in Bingham canyon porphyry (Brodebeck et al, 2020).

Covellite

Covellite is another member of the Cu-Fe-S ternary system and is commonly formed via the replacement of the earlier precipitated sulphide species such as chalcopyrite, bornite and sometimes digenite (Adegoke et al, 2021). This study indicates similar behaviour observed in Adegoke et al, 2021 as seen through petrographic observations of small specks along boundaries of bornite grains (Figure 5 and 10). These small grains of covellite when studied under LA-ICP-MS show significant elevation of trace elements particularly Ag and Bi as seen in Figure 10. These elevations show comparative elevation when compared to the bornite grains that are typically the reservoirs for these trace elements. This elevation closely mirrors that of the relationship between digenite and bornite and redistribution of trace elements under changing hydrothermal conditions.

Pyrite

Whilst pyrite is not an important mineral concerning copper grade within the Carrapateena ore deposit, its importance concerning trace element content and paragenesis of ore formation is profound. Observations of pyrite within samples of this study are restricted to depth intervals 919, 923 and 966 and only occur as inclusions, encompassed by copper sulphides such as chalcopyrite and bornite (Figure 4 and 5). Pyrite is not observed as free grains in this study. Paragenetically, pyrite is precipitated at the onset of hydrothermal activity with early magnetite (Sawyer, 2014). Precipitation

of economic minerals such as chalcopyrite and bornite are assisted by the breakdown of pre-existing pyrite to provide adequate sulphur saturation and allow cu sulphide nucleation (Hitzmann et al, 1992., Williams et al, 2005., Sawyer, 2014). The replacement and overgrowth within Carrapateena of pyrite grains to assist economic mineral growth is observed in the textures presented within Figures (5 and 6). On a trace element scale, Pyrite grains are the significant hosts for the elements Ni (1483 ppm 919) and Co (201 ppm 919) as seen in Table 3. These elements show a small degree of mineral zonation within the pyrite grains themselves with the cores more enriched than the outer rims. Bi is observed with minor concentration up to 46.2 PPM in some pyrite grains, typically a strong association around the rims of the grain in the parent chalcopyrite. Many trace elements are well known and documented for their pyrite association and typically partition via substitution into the crystal lattice such as the case of Ni and Co, whereas Bi assimilates as microparticles within the crystal structure and along defects (Cook & Chryssoulis, 1990., Reich et al, 2005., Steadmann et al, 2021). High temperature (>300ºC) precipitated pyrite is associated with greater concentrations of key elements such as Co, Ni and Bi as shown by Steadmann et al, 2021 and LA-ICP-MS analysis of samples gathered from the Intercept Hill IOCG deposit.

CONCLUSIONS

The paragenetic and trace element data obtained in this study provides evidence for a complex evolution of Cu sulphide species within the Carrapateena deposit. Textural relationships show the paragenetic progression from early pyrite to the main Cu mineralisation stages of chalcopyrite and subsequent replacing bornite. Postdating this main mineralisation stage, evidence of significant cooling within the system through

multiple overgrowth and exsolution products such as digenite and covellite and chalcopyrite show that main Cu mineralisation stage experienced multiple hydrothermal fluids of varying temperature and pH at different depth intervals. This has resulted in significant exchange and leaching of trace elements such as Ag and Bi and major elements such as Cu between sulphide species across the deposit.

Trace element analysis of each sulphide species indicates that bornite is a significant reservoir for important trace elements such as Ag and Bi across the multiple bornite zones of the deposit. However, at depth (1150m) bornite was found to lose its ability to hold significant quantities of trace elements due to the preferential formation and overgrowth of digenite at lower temperatures which incorporated these elements instead. Chalcopyrite was found to be a poor host for significant quantities of the trace elements across the multiple intervals examined in the study except for instances of pyrite inclusions within larger parent chalcopyrite grains. Replacement and overgrowth of bornite via chalcopyrite was also observed resulting in typically trace element enriched bornite being exsolved to heavily depleted chalcopyrite with Ag, Bi and Cu lost within the low temperature fluids (125-250ºC) associated with these exsolution textures. This evidence presented in this study provides sufficient cause for the mineralisation of Carrapateena's Cu sulphides to be a result of multiple hydrothermal fluids of varying temperature and pH with main stage mineralisation at >250ºC and basic pH to low temperature replacement and overgrowth occurring at 125-250ºC with varying pH levels driving the replacement products.

ACKNOWLEDGMENTS

I would like to thank my supervisors Dr. Richard Lilly, Prof. Martin Hand and Shaun Light for all their time, patience and invaluable tips and advice throughout the year. To the Playford Trust and OZ Minerals for their generous financial support towards the undertaking and completion of my project. Also, to Aoife McFadden and Sarah Gilbert at Adelaide Microscopy thank you for your assistance and patience during data collection. A special thank you to my girlfriend Maddie for her support during these restricted COVID times. Finally, a sincere thank you to the whole Honours cohort for making this a fantastic final year of university.

REFERENCES

ADEGOKE, IA, XIA, F, DEDITIUS, AP, PEARCE, MA, ROBERTS, MP & BRUGGER, J 2021, 'A new mode of mineral replacement reactions involving the synergy between fluid-induced solid-state diffusion and dissolution-reprecipitation: A case study of the replacement of bornite by copper sulfides', *Geochimica et Cosmochimica Acta*.

BARTON, M, 2014, 'Iron Oxide(–Cu–Au–REE–P–Ag–U–Co) Systems', *Treatise on Geochemistry*, vol. 2, pp. 515-541

BRODBECK, M., MCCLENAGHAN, S., KAMBER, B. S., AND REDMOND, P. 2020 'Energy Critical Element and Precious Metal Deportment in Cu-(Fe-) Sulphides from the Bingham Canyon Porphyry Cu-Mo-Au Deposit', EGU General Assembly 2020, Online, 4–8 May 2020, EGU2020-22017

CLARK, J & EHRIG, K, 2020, 'The Olympic Dam Cu-U-Au-Ag deposit, Unravelling the giant', *NExUS invited talk presentation*

COOK, NJ & CHRYSSOULIS, SL 1990, 'Concentrations of invisible gold in the common sulfides', *Canadian Mineralogist*, vol. 28, pp. 1–16

COOK, NJ, CIOBANU, CL, DANYUSHEVSKY, LV & GILBERT, S 2011, 'Minor and trace elements in bornite and associated Cu–(Fe)-sulfides: A LA-ICP-MS study Bornite mineral chemistry', *Geochimica et Cosmochimica Acta*, vol. 75, no. 21, pp. 6473–6496.

CORRIVEAU, L., POTTER, E.G., MONTREUIL, J.-F., BLEIN, O., EHRIG, K., FABRIS, A, & REID, A, 2019, 'Alteration facies in 'IOCG terranes': a global view on mineral systems with IOCG and affiliated deposit types', *Geological Survey of South Australia, Discovery Day 2019*

CORRIVEAU, L., 2007, 'Iron oxide copper-gold (±Ag±Nb±P±REE±U) deposits: a Canadian perspective', *Mineral Deposits of Canada: A Synthesis of Major Deposit-Types, District Metallogeny, the Evolution of Geological Provinces, and Exploration Methods: Geological Association of Canada*, Mineral Deposits Division, Vol. 5, pp.265-278.

DANYUSHEVSKY L.V., ROBINSON P., GILBERT S, NORMAN M., LARGE R., MCGOLDRICK P., SHELLEY J.M.G. (2011) Routine quantitative multi-element analysis of sulphide minerals by laser ablation ICP-MS: Standard development and consideration of matrix effects. Geochemistry: Exploration, Environment, Analysis, 11, p. 51-60

FABRIS, A, 2020, 'Alteration trends and geochemical characteristics of IOCG deposits in the Olympic Cu-Au Province', *NEXUS presentation*, Geological Survey of South Australia

FANNING, C. M., ET AL. (1988). "Refined Proterozoic evolution of the Gawler Craton, South Australia, through U-Pb zircon geochronology." *Precambrian Research*, vol. 40-41, pp. 363-386.

GEORGE, LL, COOK, NJ, CROWE, BBP & CIOBANU, CL 2018, 'Trace elements in hydrothermal chalcopyrite', *Mineralogical Magazine*, vol. 82, no. 1, pp. 59–88.

GEORGE, LL 2017, *Trace element distributions and partitioning trends in hydrothermal base metal sulphide ores comprising sphalerite, galena, chalcopyrite and tetrahedrite-tennantite*.

GOW, PA, WALL, VJ, OLIVER, NHS & VALENTA, RK 1994, 'Proterozoic iron oxide (Cu-U-Au-REE) deposits; further evidence of hydrothermal origins', *Geology (Boulder)*, vol. 22, no. 7, pp. 633–636.

GROVES, DI, BIERLEIN, FP, MEINERT, LD & HITZMAN, MW 2010, 'Iron oxide copper-gold (IOCG) deposits through Earth history; implications for origin, lithospheric setting, and distinction from other epigenetic iron oxide deposits', *Economic Geology and the Bulletin of the Society of Economic Geologists*, vol. 105, no. 3, pp. 641–654.

HITZMAN, MW, ORESKES, N & EINAUDI, MT 1992, 'Geological characteristics and tectonic setting of Proterozoic iron oxide (Cu-U-Au-REE) deposits', *Precambrian Research*, vol. 58, no. 1, pp. 241–287.

HAND, M, REID, A & JAGODZINSKI, L, 2007, 'Tectonic framework and related Evolution of the Gawler craton, South Australia' *Economic Geology*, vol. 102, pp. 1377-1395

HITZMAN, M & VALENTA, R, 2005, ' Uranium in Iron Oxide- Copper-Gold (IOCG) systems', *Economic Geology*, vol. 100, pp. 1657-1661

JAIRETH, S, HOATSON, D & MIEZITIS, Y ,2014, 'Geological setting and resources of the major rare earth element deposits in Australia', *Ore Geology Review*, vol.62, pp.72-128

KLEEMAN, A 2012, 'The petrology and trace element geochemistry of the Carrapateena deposit, Olympic IOCG province, South Australia', *Honours Thesis*, University of Tasmania
LI, K, BRUGGER, J & PRING, A 2018, 'Exsolution of chalcopyrite from bornite-digenite solid solution: an example of a fluid-driven back-replacement reaction', *Mineralium Deposita*, vol. 53, no. 7, pp. 903–908.

LLOYD, JC, BLADES, ML, COUNTS, JW, COLLINS, AS, AMOS, KJ, WADE, BP, DRABSCH, M 2020, 'Neoproterozoic geochronology and provenance of the Adelaide Superbasin', *Precambrian Research*, vol. 350, p. 105849–.

MOONEY, A, 2018, 'Carrapateena project update', AusIMM presentation

NEUMANN, M, 2019, 'IOCG Workshop: Stuart Shelf hematite rich end members', *Geological Survey South Australia presentation*.

OZ MINERALS, 2020, *ASX Quarterly Release*

PORTER, T, 2010, 'Hydrothermal Iron Oxide Copper-Gold and Related Deposits: A Global Perspective - Advances in the Understanding of IOCG Deposits', Vol. 3, PGC Publishing, Adelaide.

REICH, M, DEDITIUS, A, CHRYSSOULIS, S, LI, J-W, MA, C-Q, PARADA, MA, MITTERMAYR, F 2013, 'Pyrite as a record of hydrothermal fluid evolution in a porphyry copper system: A SIMS/EMPA trace element study', Geochimica et Cosmochimica Acta, vol. 104, pp. 42–62.

REYNOLDS, L.J. 2000, 'Geology of the Olympic Dam Cu-U-Au-Ag-REE Deposit', *Hydrothermal Iron Oxide Copper-Gold & Related Deposits: A Global Perspective*, Vol. 1, pp 93-104.

REID, A 2019, 'The Olympic Cu-Au Province, Gawler Craton: A Review of the Lithospheric Architecture, Geodynamic Setting, Alteration Systems, Cover Successions and Prospectivity', *Minerals*, vol. 9, no. 371, pp 1-37

ROLLOG, M, COOK, NJ, GUAGLIARDO, P, EHRIG, K, CIOBANU, CL & KILBURN, M 2019, 'Detection of Trace Elements/Isotopes in Olympic Dam Copper Concentrates by nanoSIMS', *Minerals (Basel)*, vol. 9, no. 6, p. 336

SAWYER, M 2014, 'Geology of Carrapateena' (*Internal Oz Report*)

SAWYER, M, WHITTAKER, B & DE LITTLE, J, 2017, ' Carrapateena Iron Oxide Cu-Au-Ag-U deposit', *Australian Ore deposits*, pp. 615

SCHLEGEL, T. U., WAGNER, T., BOYCE, A., AND HEINRICH, C. A., 2017, 'A magmatic source of hydrothermal sulfur for the Prominent Hill deposit and associated prospects in the Olympic iron oxide copper-gold (IOCG) province of South Australia', *Ore Geology Reviews*, vol. 89, p. 1058-1090

SCHLEGEL, T, WAGNER, T & FUSSWINKEL, T, 2019, 'Fluorite as indicator mineral in Iron oxide-copper-gold systems: explaining the IOCG deposit diversity', *Chemical Geology*, vol.548, pp.

SHAOFENG, L & SHUIXING, F 2016, 'A Research Review of Iron Oxide Copper-Gold Deposits', *Acta Geologica Sinica (Beijing)*, vol. 90, no. 4, pp. 1341–1352.

SKIRROW, RG, WIELEN, SE, CHAMPION, DC, CZARNOTA, K & THIEL, S 2018, 'Lithospheric Architecture and Mantle Metasomatism Linked to Iron Oxide Cu-Au Ore Formation: Multidisciplinary Evidence from the Olympic Dam Region, South Australia', *Geochemistry, Geophysics, Geosystems : G3*, vol. 19, no. 8, pp. 2673–2705.

STEADMAN, JA, LARGE, RR, OLIN, PH, DANYUSHEVSKY, LV, MEFFRE, S, HUSTON, D & WELLS, T 2021, 'Pyrite trace element behavior in magmatic-hydrothermal environments: An LA-ICPMS imaging study', *Ore Geology Reviews*, vol. 128.

TAYLOR, R, 2014, 'Paragenesis, ore textures and general observations, Carrapateena prospect', Tasmania, (Internal Oz report)

TIDDY, C & GILES, D, 2020, 'Suprasubduction zone model for metal endowment at 1.60-1.57 Ga in eastern Australia', *Ore Geology Reviews*, vol. 122, https://doi.org/10.1016/j.oregeorev.2020.103483

VELLA, L & EMERSON, D (2009) Carrapateena: physical properties of a new iron-oxide copper-gold deposit, *ASEG Extended Abstracts*, vol. 1, 1-13

VERDUGO-IHL, M, CIOBANU, C, COOK, N, EHRIG, K, COURTNEY-DAVIES, L & GILBERT, S, 2017, ' Textures and U-W-Sn-Mo signatures in hematite from the Olympic Dam Cu-U-Au-Ag deposit, South Australia: Defining the archetype for IOCG deposits', *Ore Geology Reviews*, vol. 91, pp. 173-195

WILLIAMS, J, BARTON, M, JOHNSON, D, FONTBOTE, L, HALLER, A, MARK, G, OLIVER, N & MARSCHIK, R, 2015, 'Iron oxide Copper-Gold deposits: *Geology*, Space-Time distribution and possible modes of origin', Economic Geology, vol. 100, pp. 371-405

WILLIAMS, P, 2012, 'X-Ray mapping and SEM investigation of Uranium and Gold distribution in twelve samples from Carrapateena', *Clump Mountain Geoscience*, (Internal Oz report)

WILLIAMS PJ, BARTON, M, RYAN C, 2005 Iron Oxide copper gold deposit geology, space time distribution and possible modes of origin. *Economic geology*, 100th anniversary volume, 371-406

ZHANG YANG, CAI YUANFENG, QU YANG, WANG QIN, GU LIXIN & LI GAOJUN 2020, 'Two-stage fluid pathways generated by volume expansion reactions: insights from the replacement of pyrite by chalcopyrite', *Scientific Reports*, vol. 10, no. 1, pp. 19993–19993.

ZHAO, J, BRUGGER, J, NGOTHAI, Y & PRING, A 2014, 'The replacement of chalcopyrite by bornite under hydrothermal conditions', *The American Mineralogist*, vol. 99, no. 11-12, pp. 2389–2397.

ZHAO, J, BRUGGER, J, GRGURIC, BA, NGOTHAI, Y & PRING, A 2017, 'Fluid-Enhanced Coarsening of Mineral Microstructures in Hydrothermally Synthesized Bornite–Digenite Solid Solution', *ACS Earth and Space Chemistry*, vol. 1, no. 8, pp. 465–474.

APPENDIX A: LA-ICP-MS MAPS

Interval 878 Texture 1: chalcopyrite-bornite

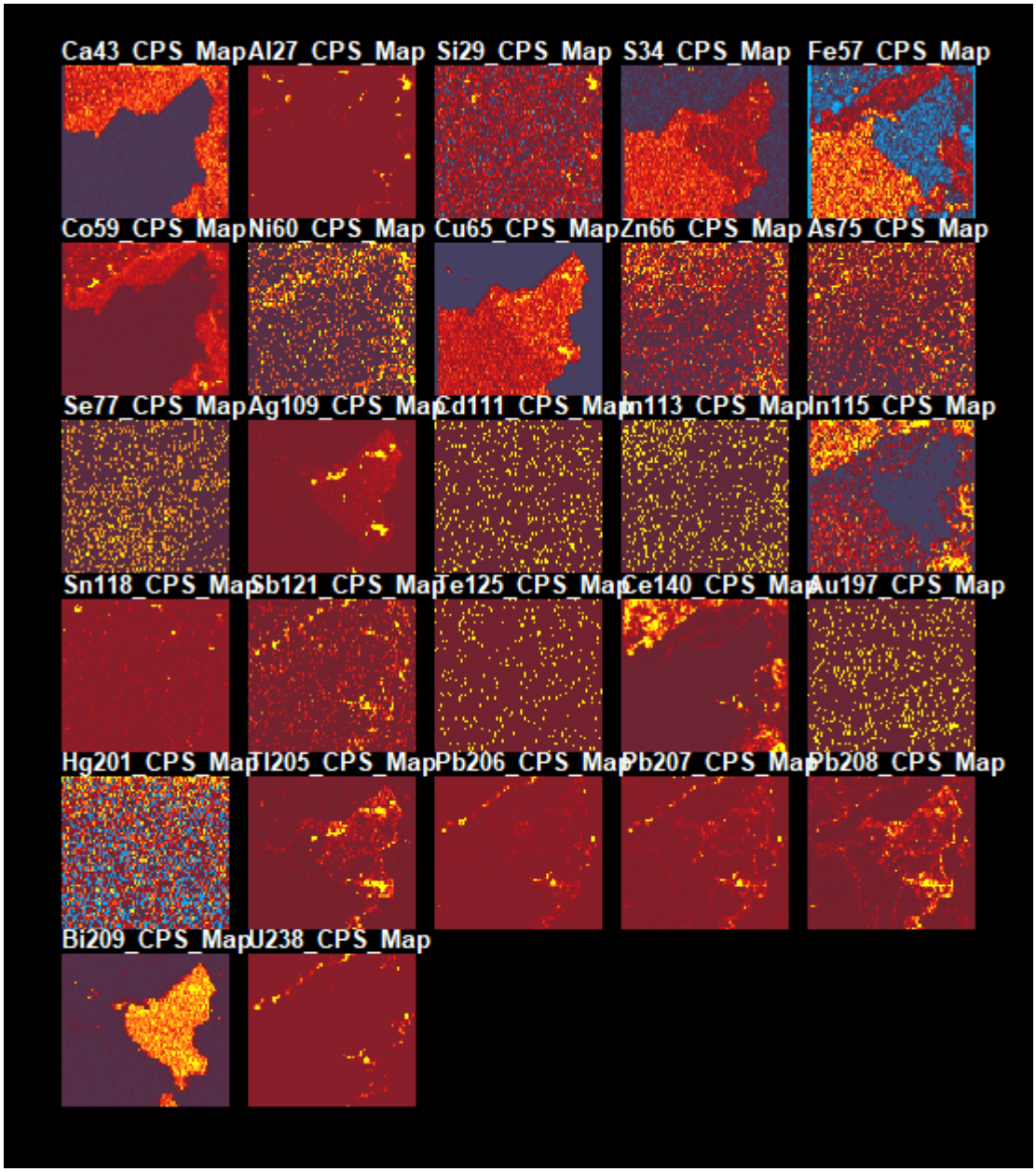

Interval 878 Texture 2: chalcopyrite-bornite

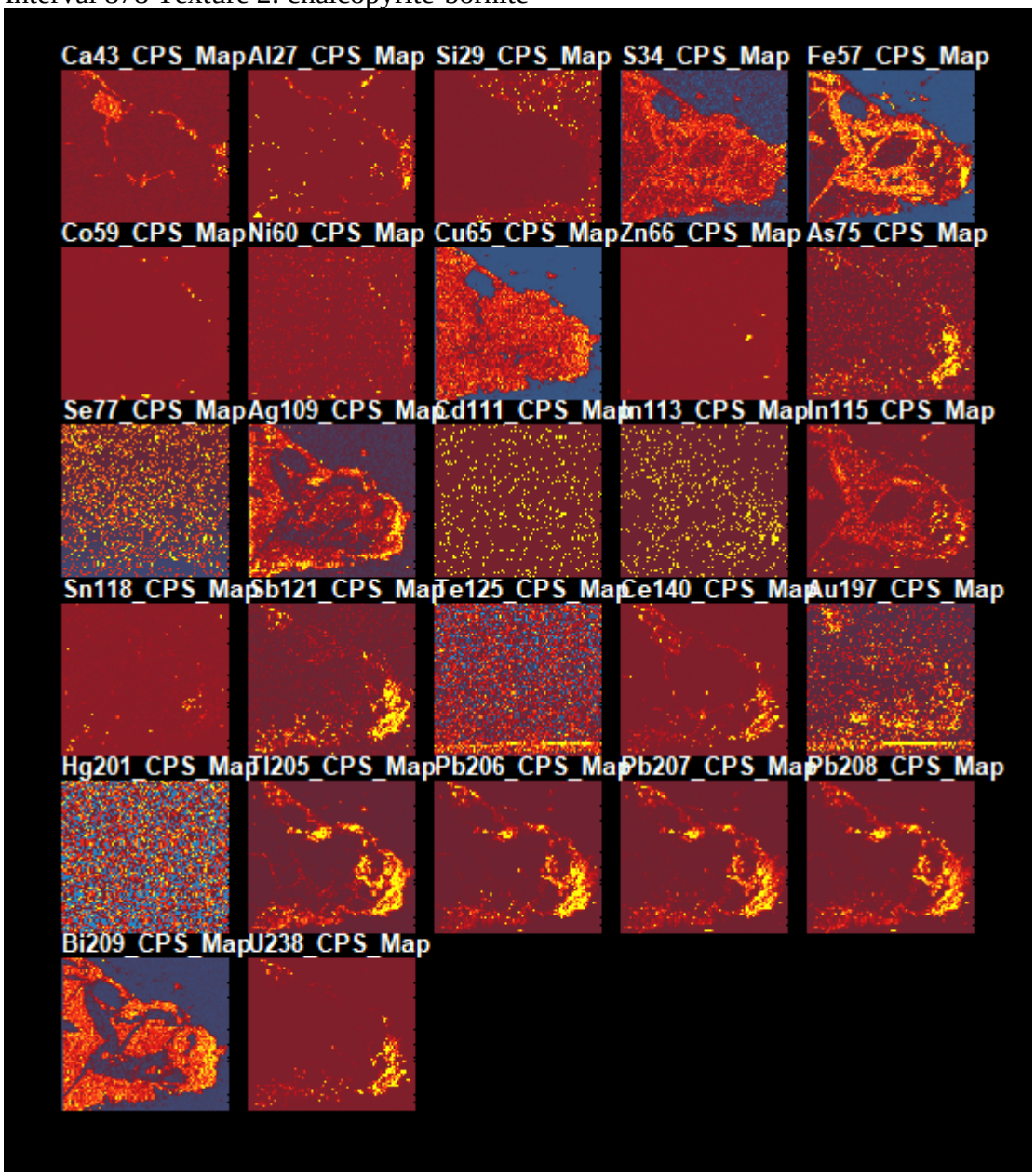

Interval 919 Texture 1: chalcopyrite-pyrite

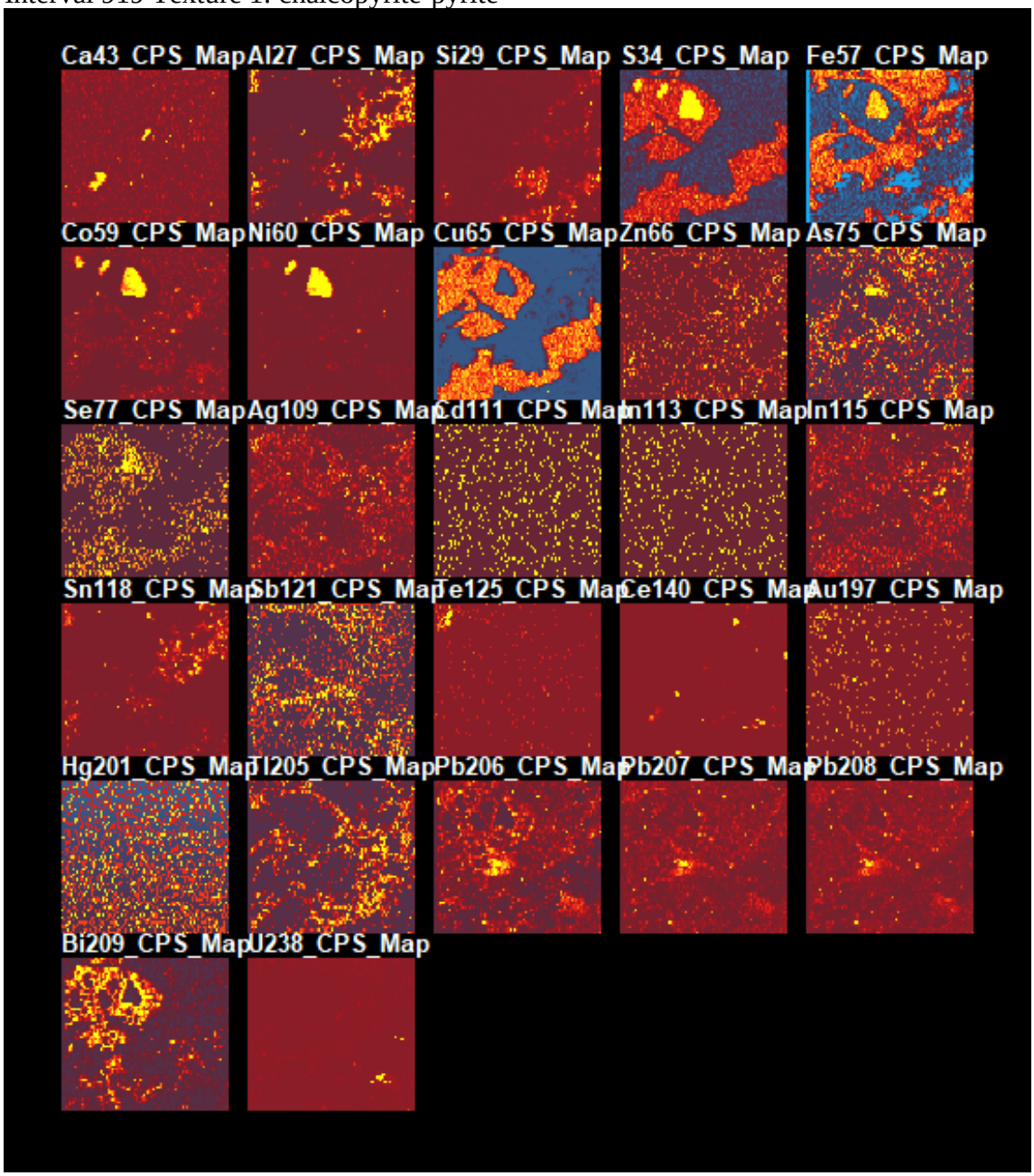

Interval 919 Texture 2: chalcopyrite-pyrite

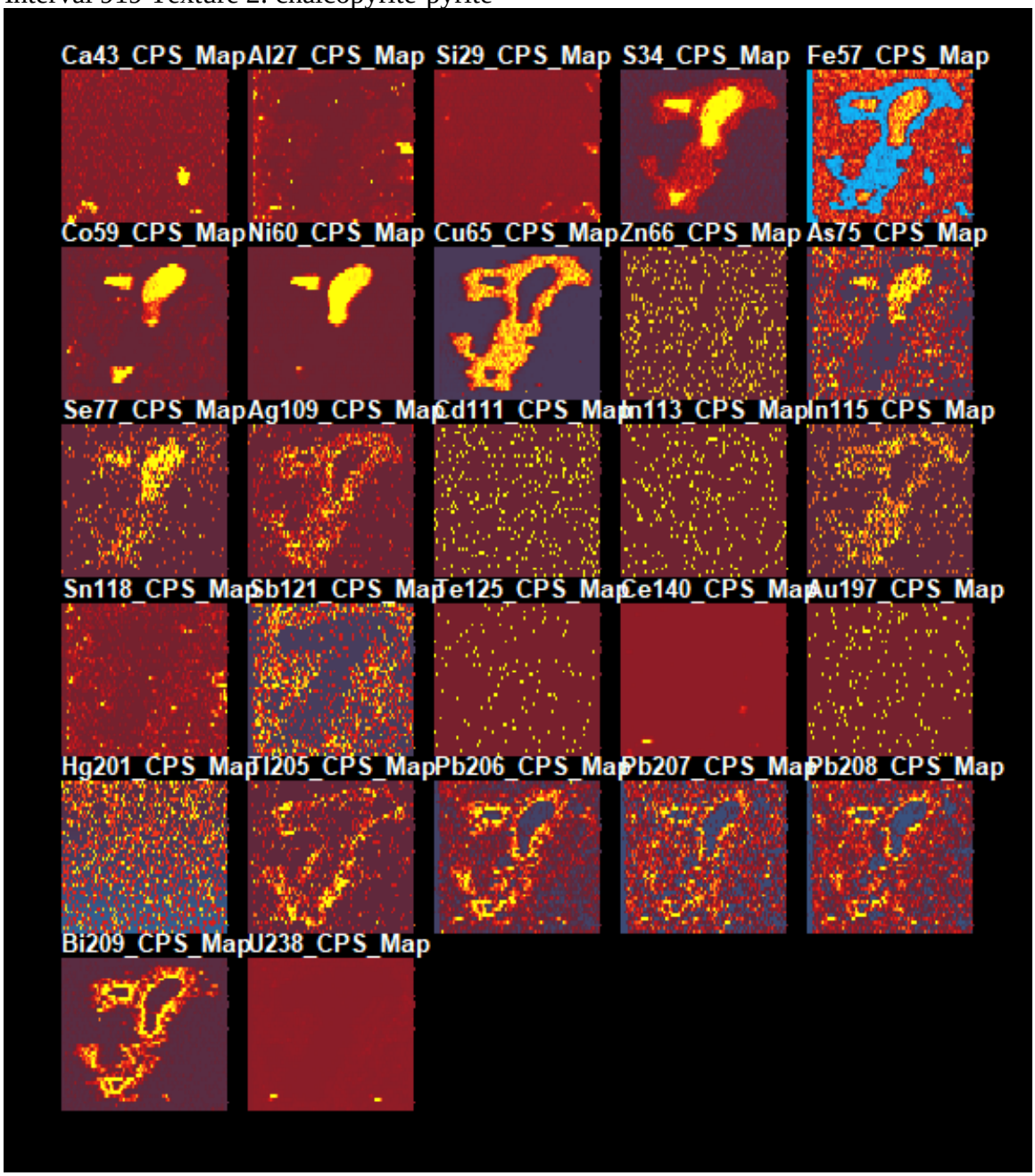

Interval 923 Texture 1: bornite-chalcopyrite

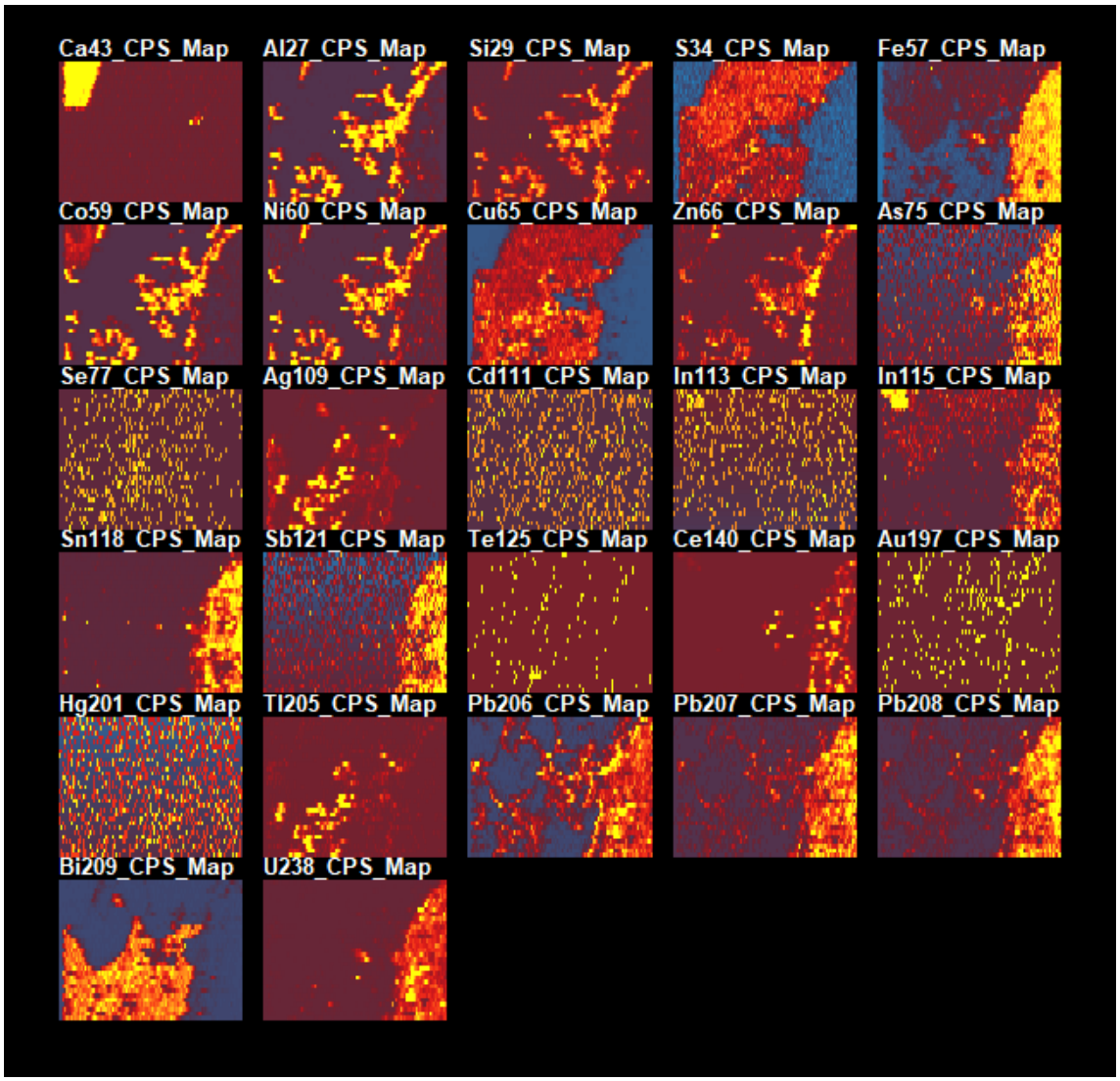

Interval 923 Texture 2: bornite-chalcopyrite

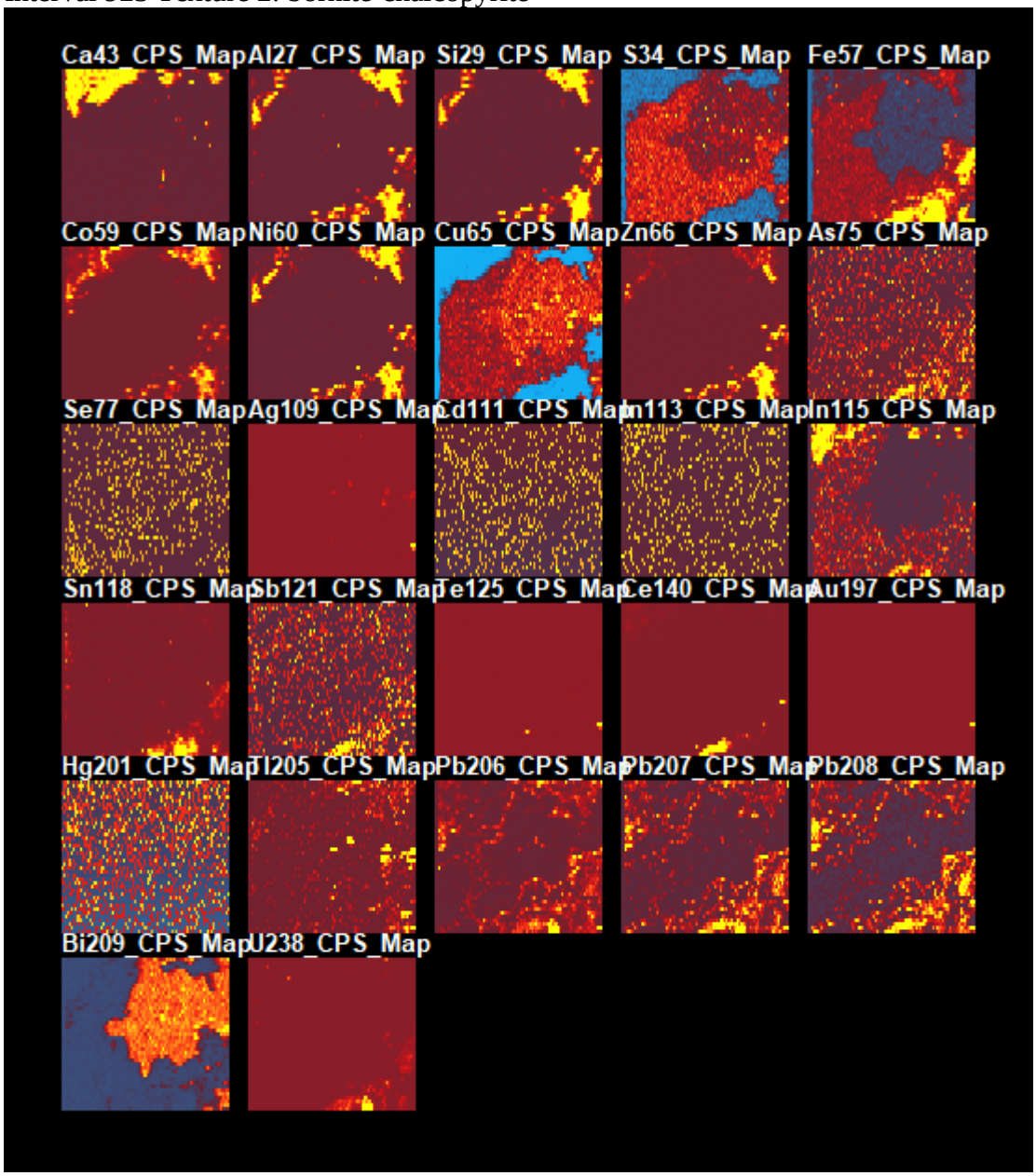

Interval 923 Texture 3: bornite-chalcopyrite

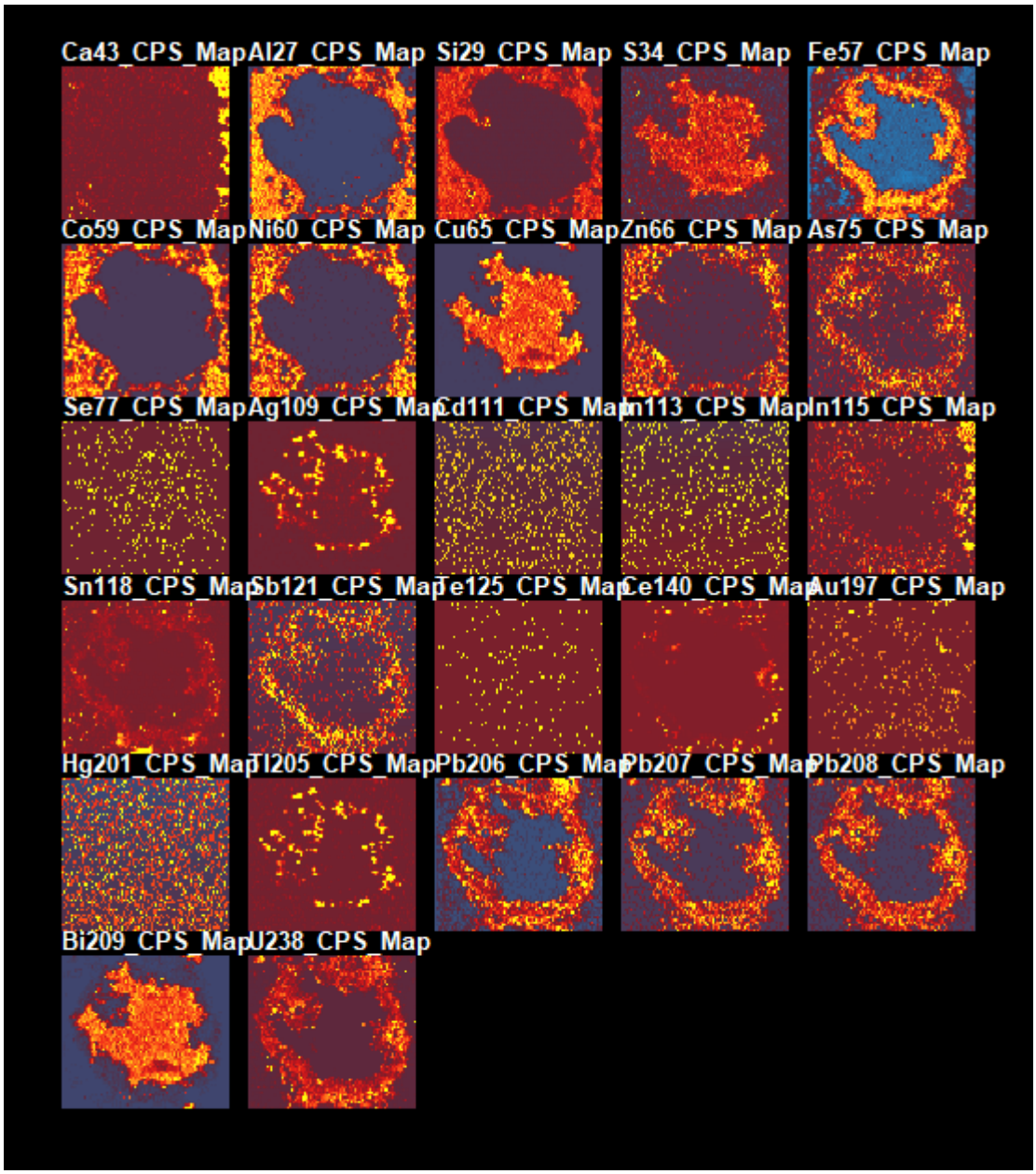

Interval 923 Texture 4: bornite-chalcopyrite

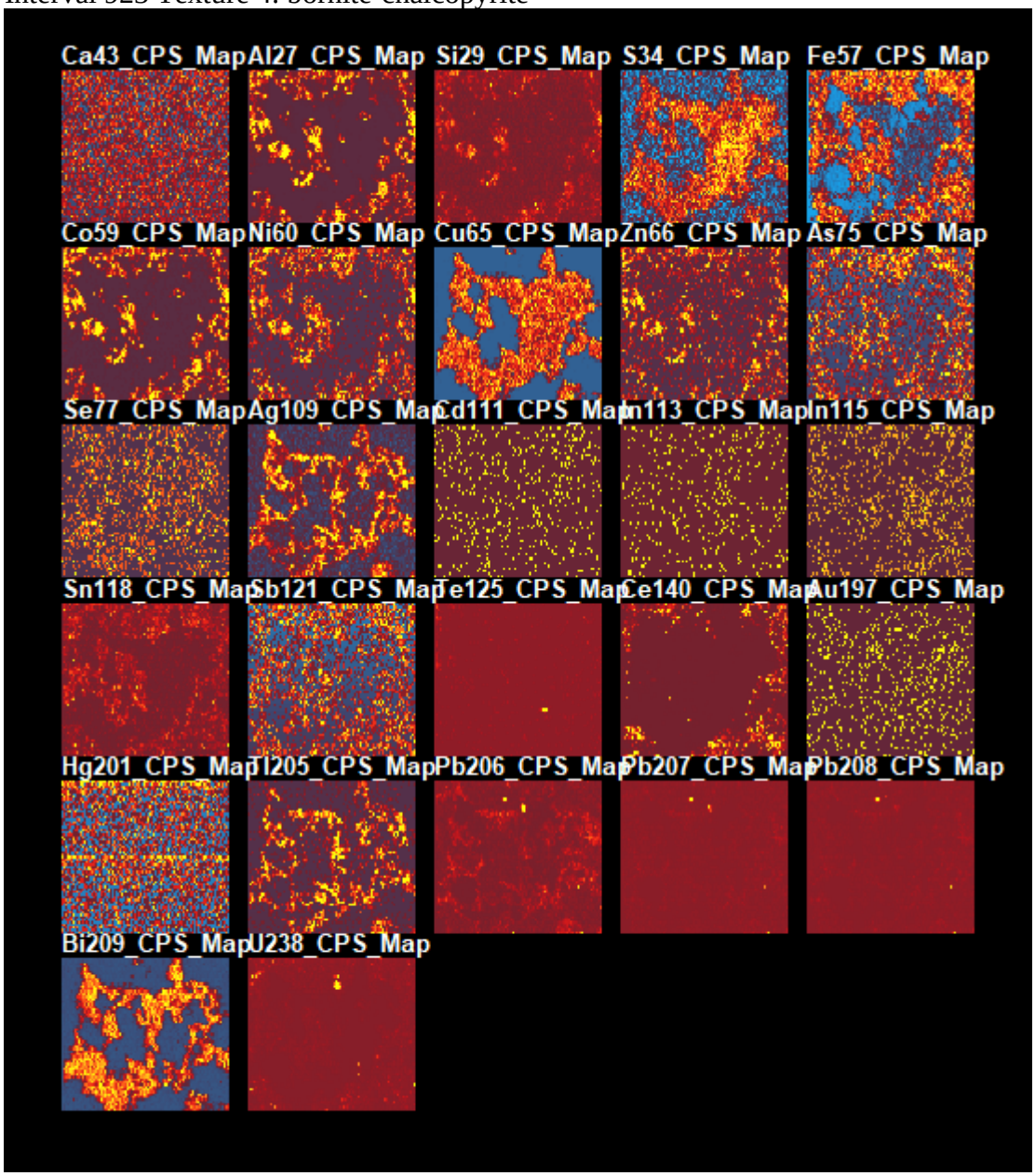

Interval 923 Texture 5: bornite-chalcopyrite

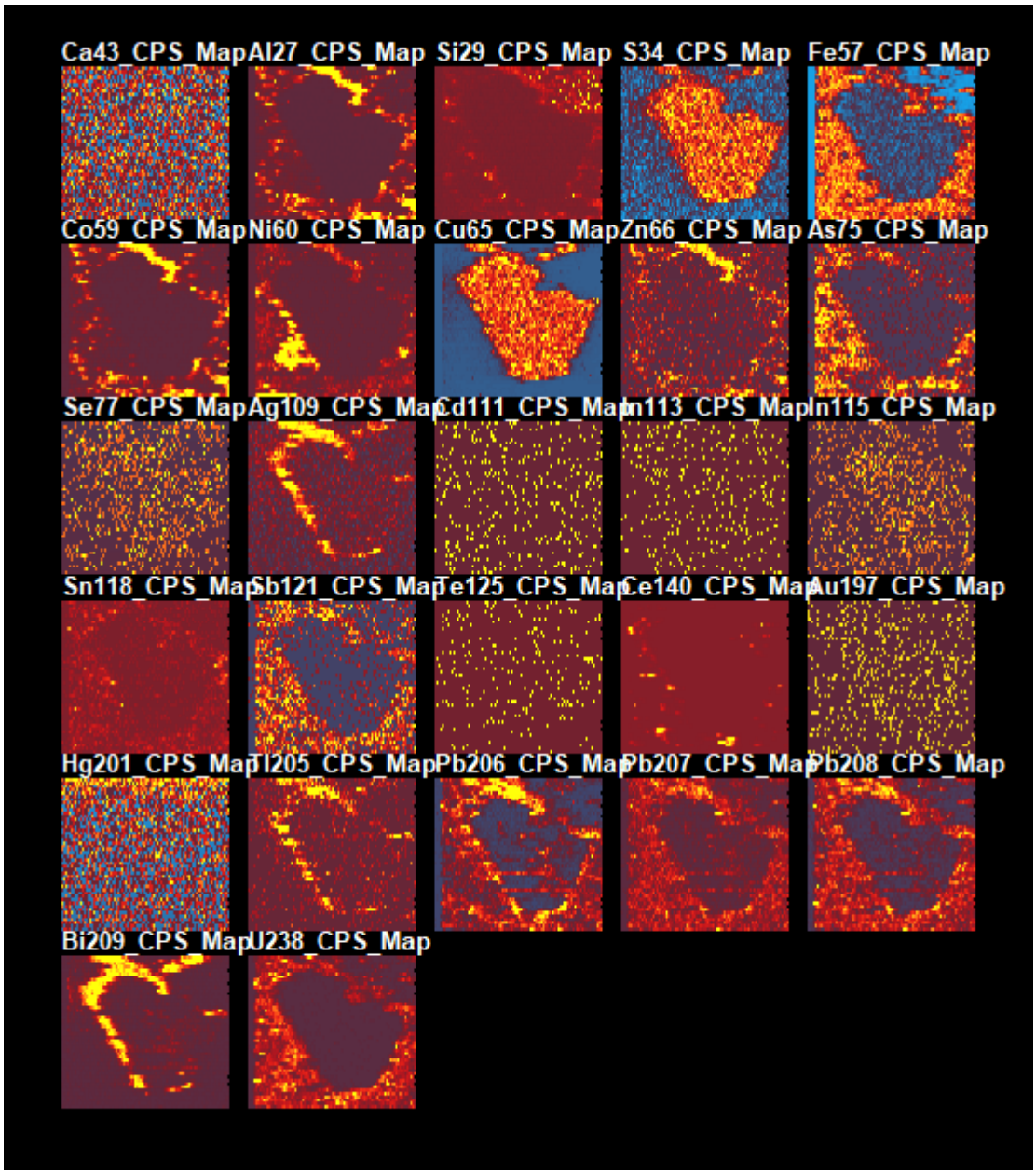

Interval 923 Texture 6: bornite-chalcopyrite

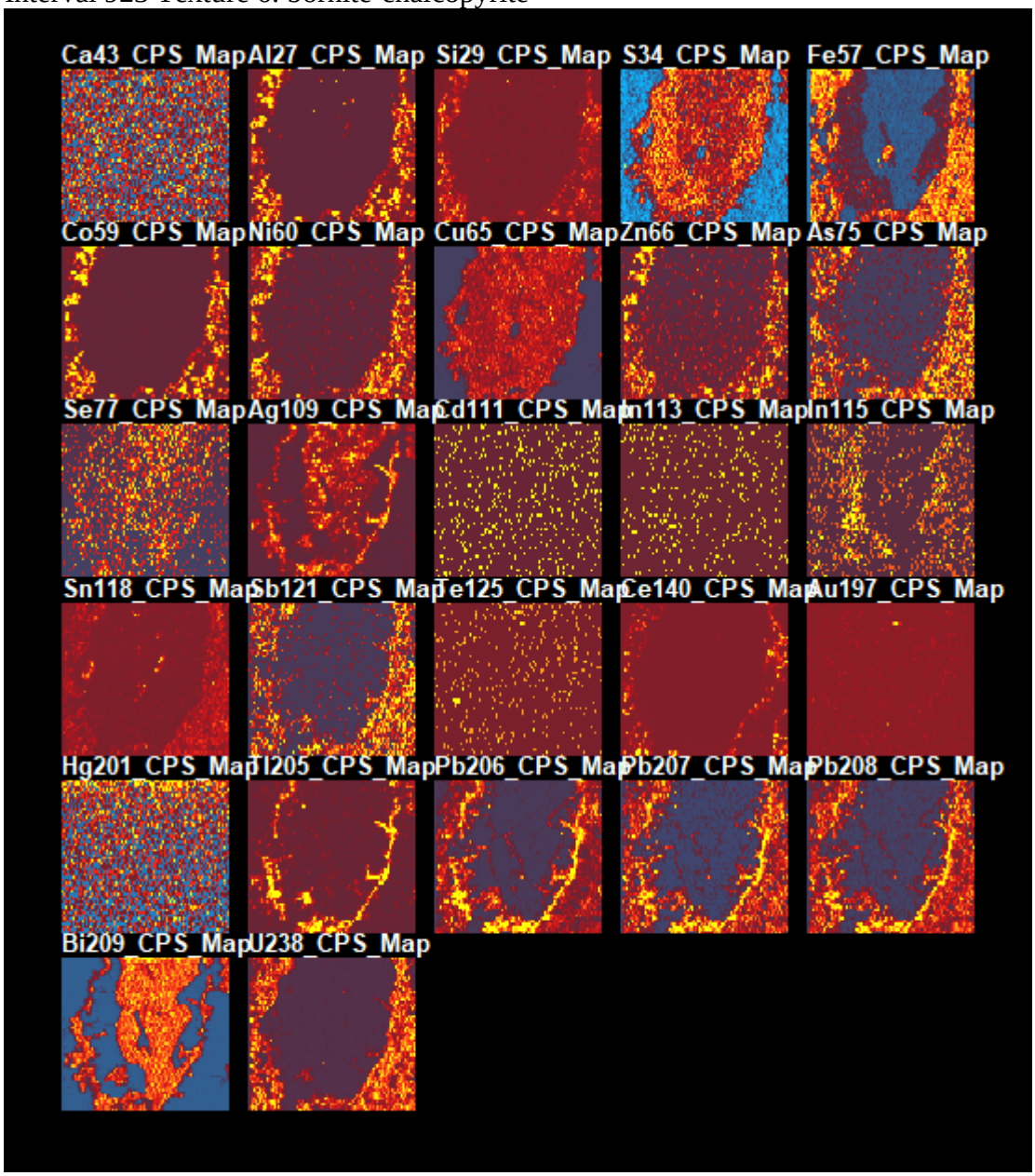

Interval 923 Texture 7: bornite-chalcopyrite

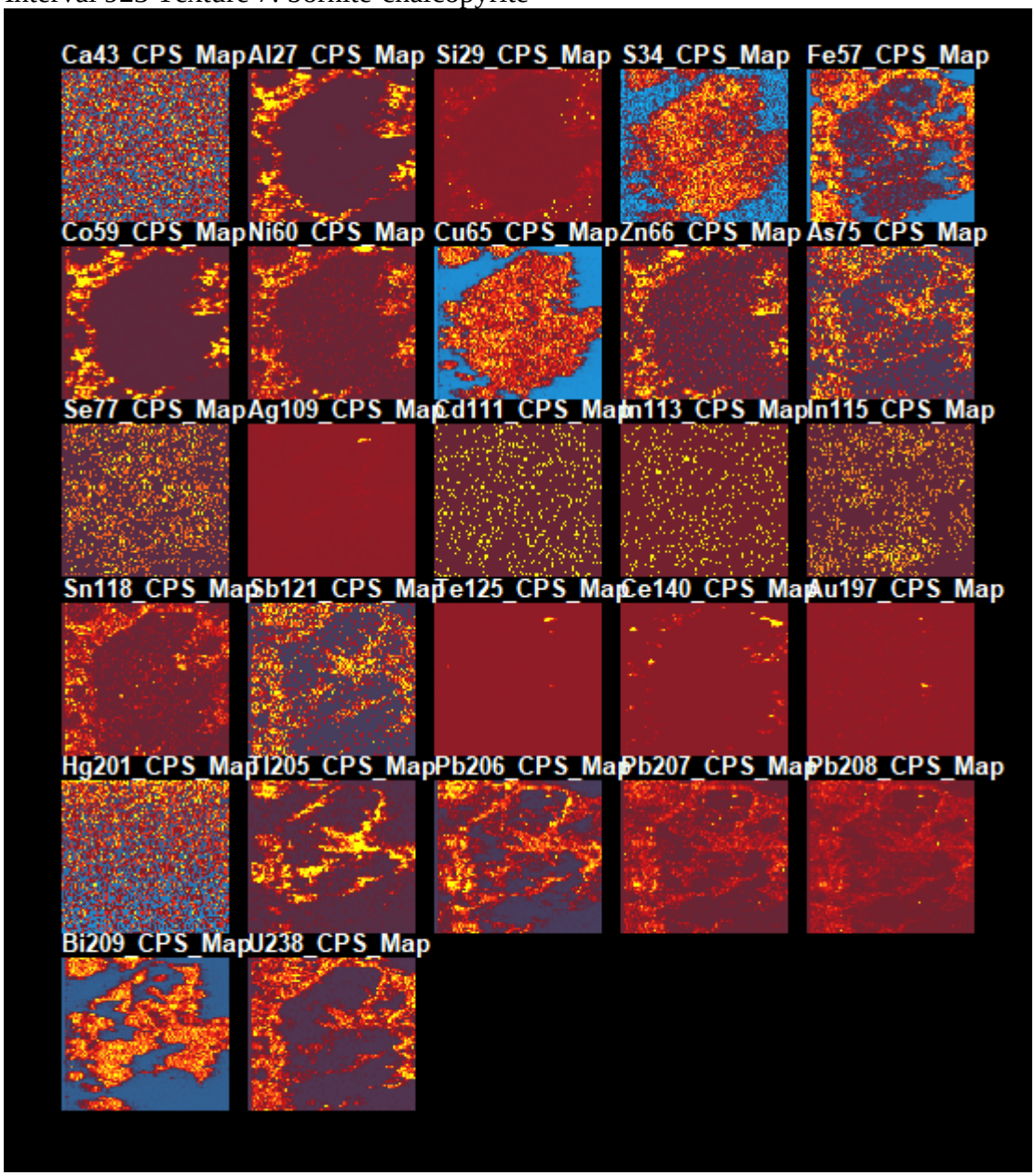

Interval 966 Texture 1: chalcopyrite-hematite

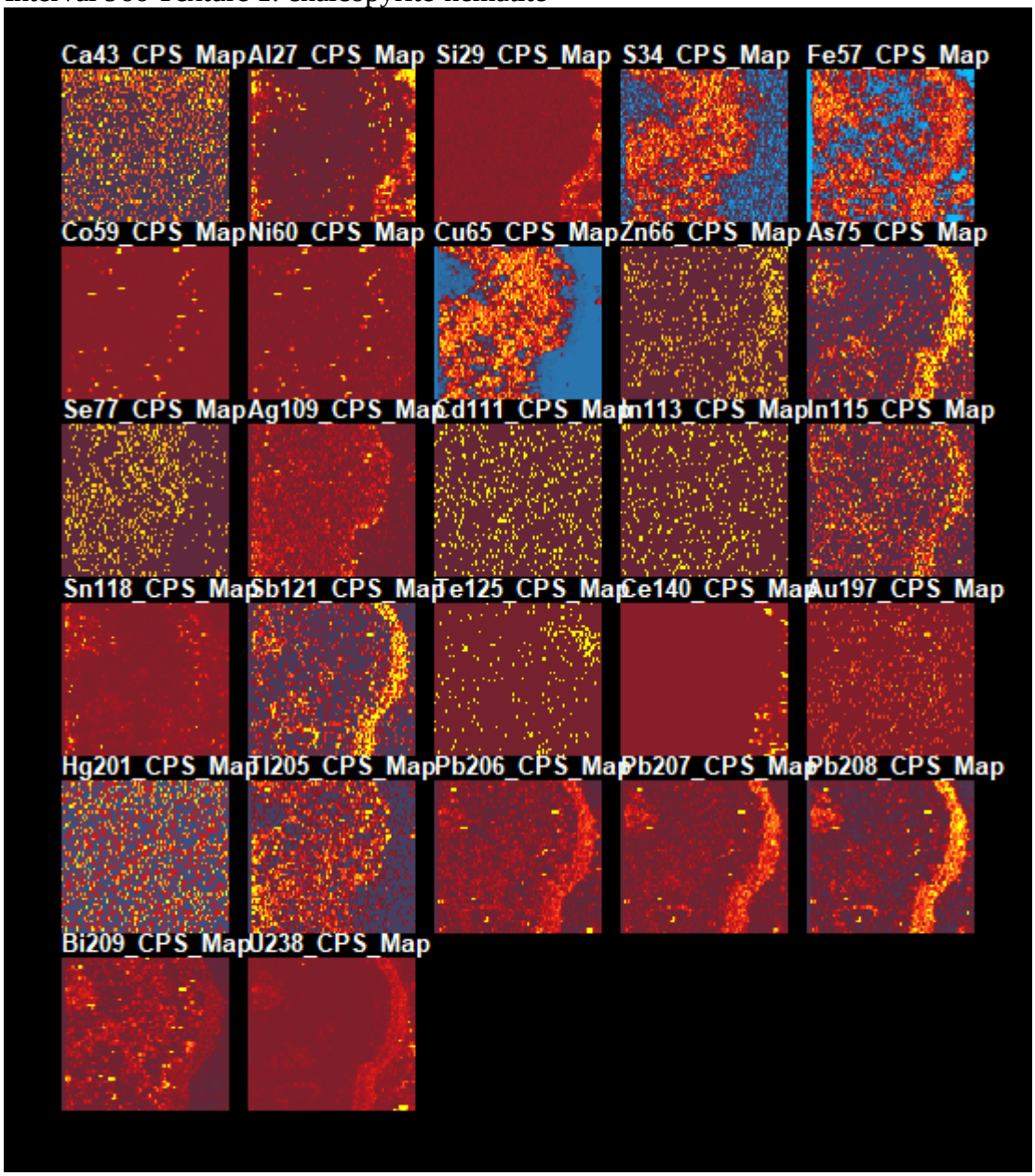

Interval 966 Texture 2: chalcopyrite-pyrite

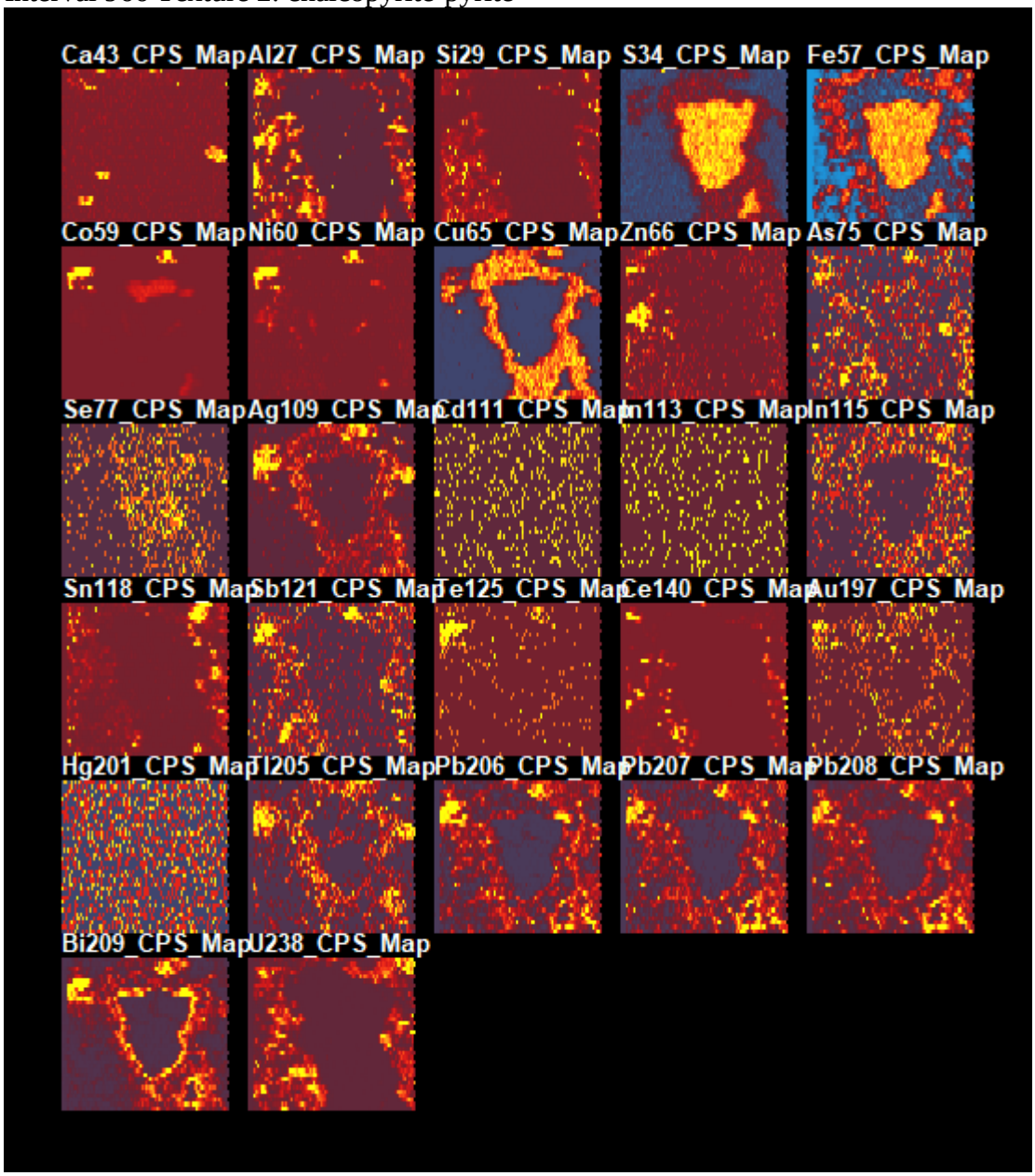

Interval 966 Texture 3: chalcopyrite-pyrite

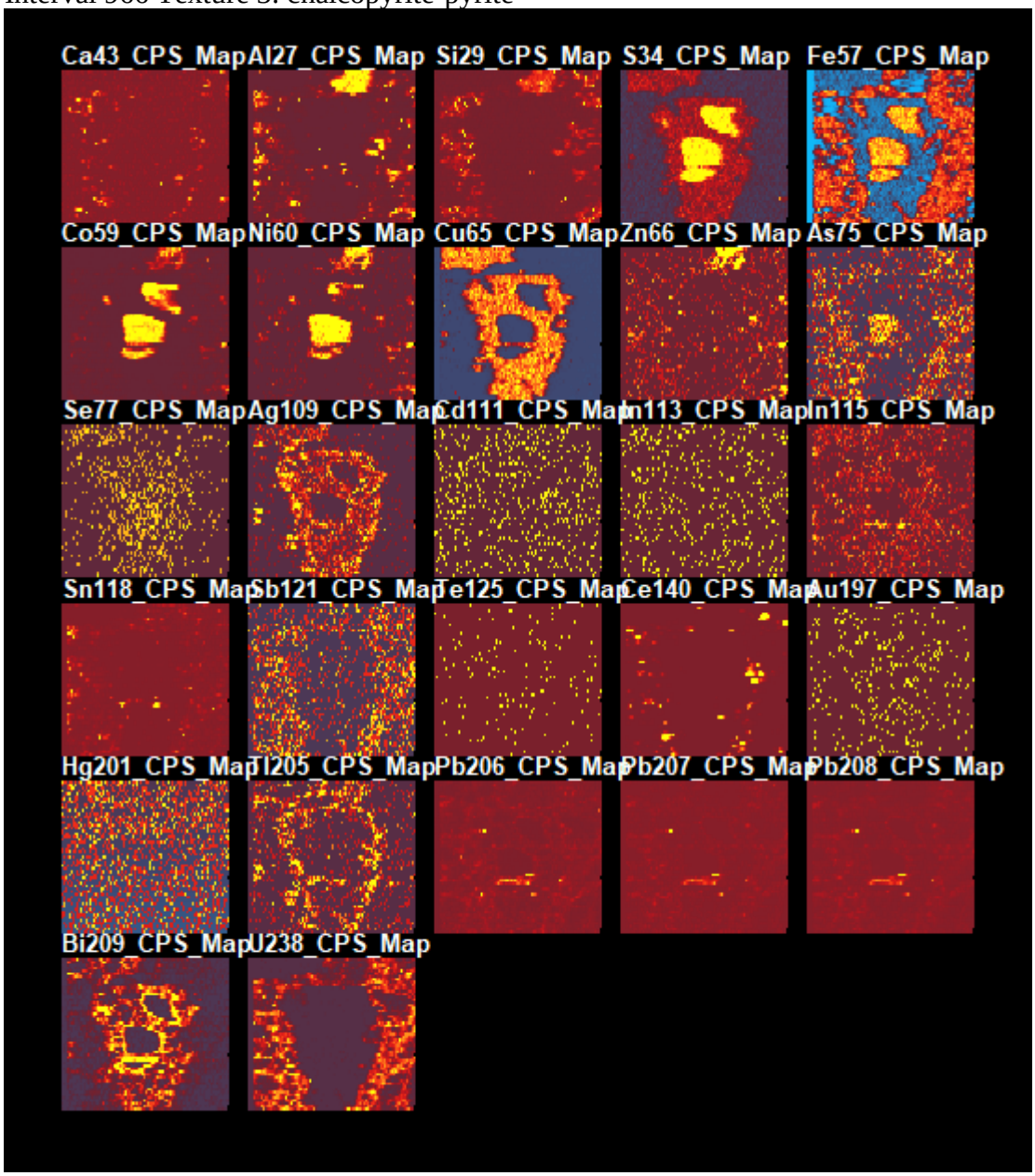

Interval 966 Texture 4: chalcopyrite-pyrite

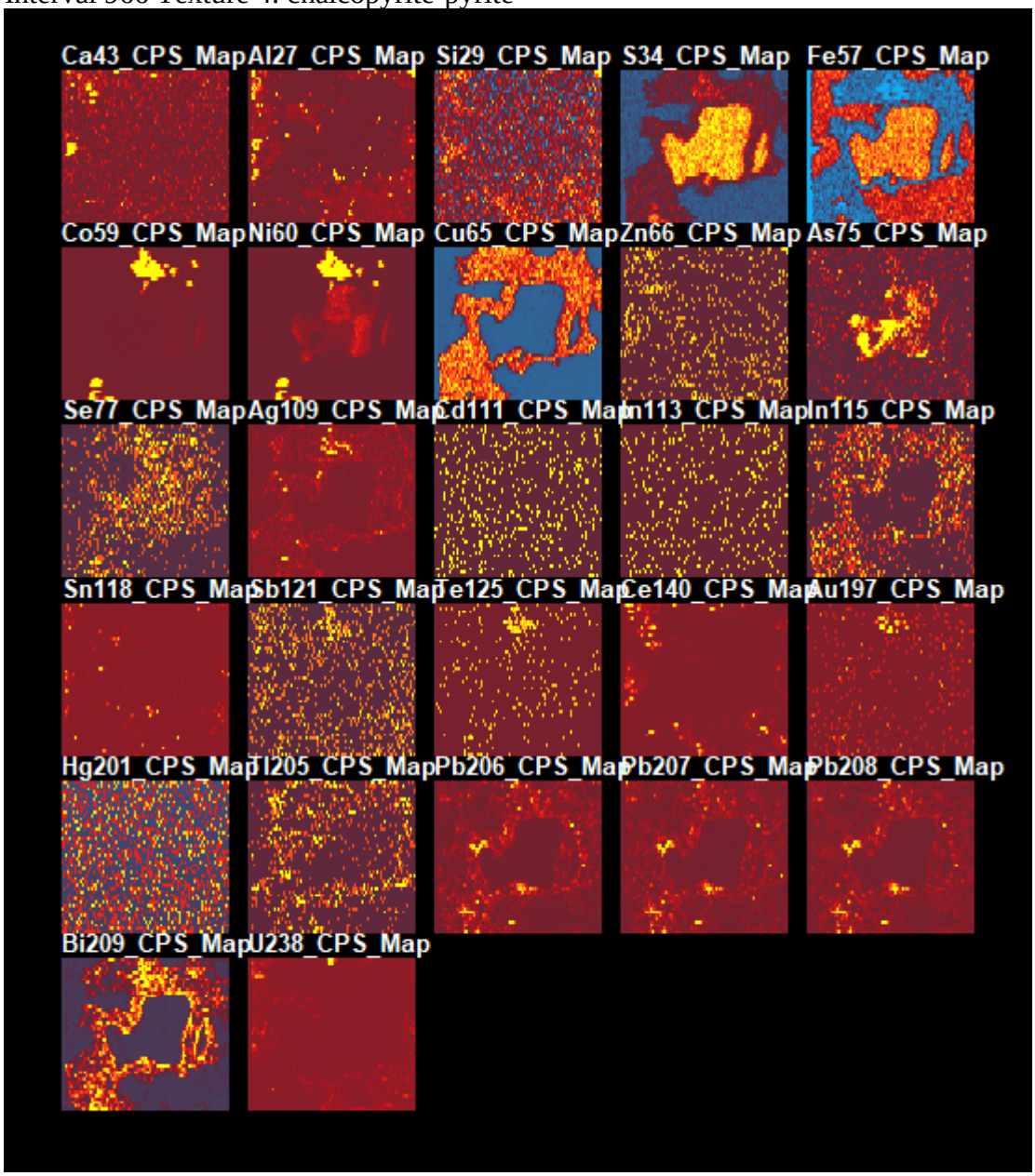

Interval 966 Texture 5: bornite-pyrite

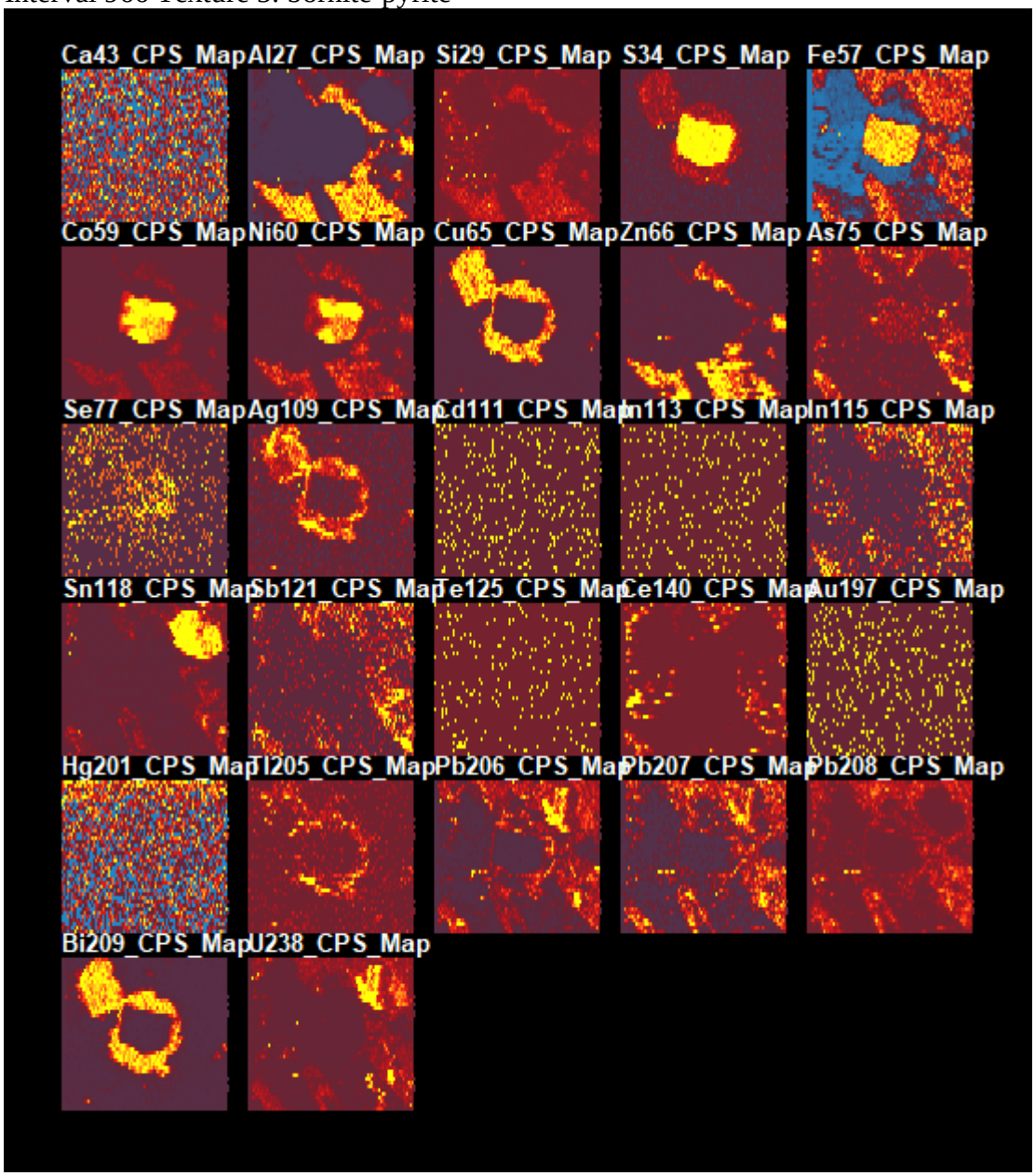

Interval 966 Texture 5: bornite-chalcopyrite

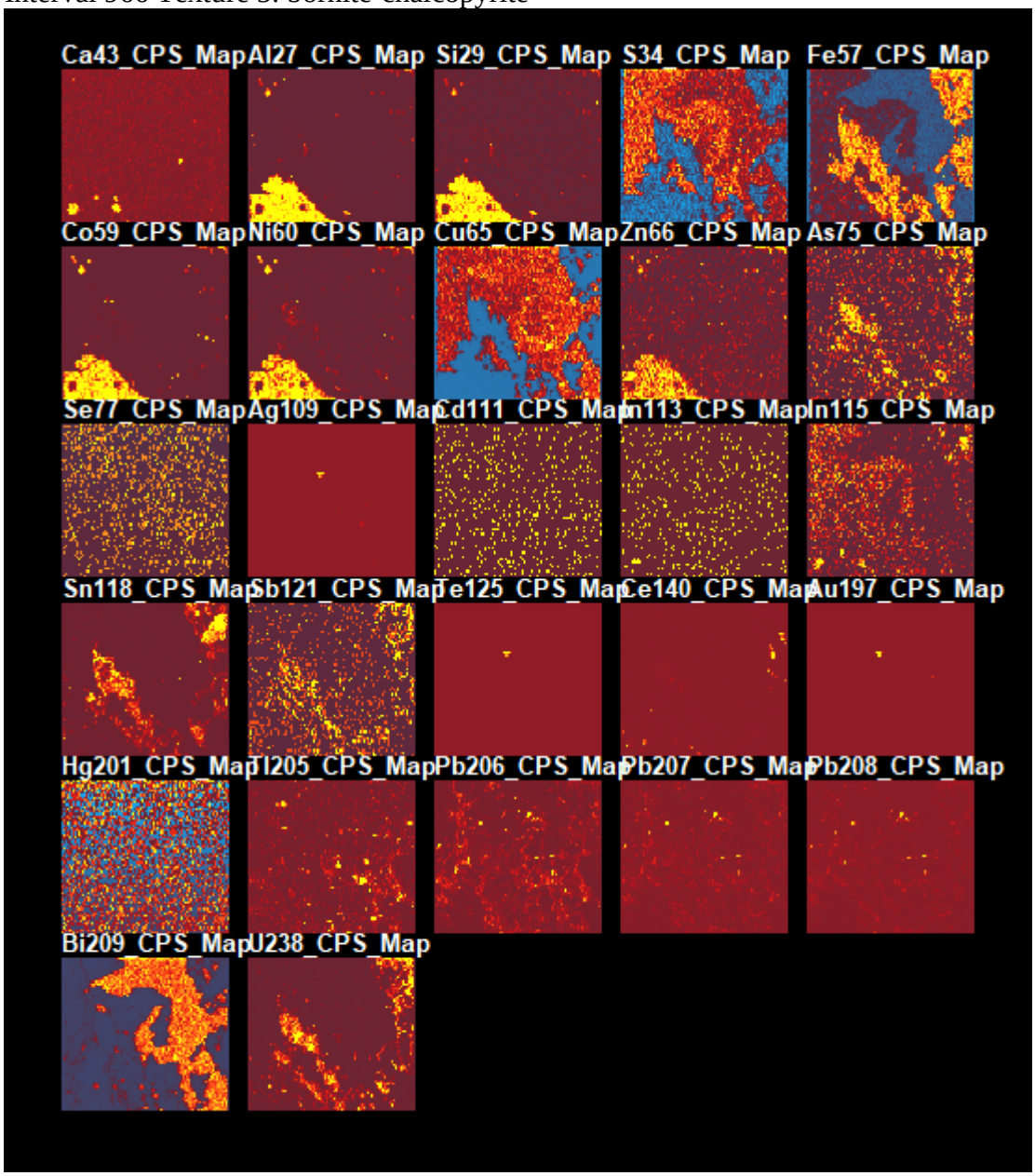

Interval 1099 Texture 1: chalcopyrite-bornite

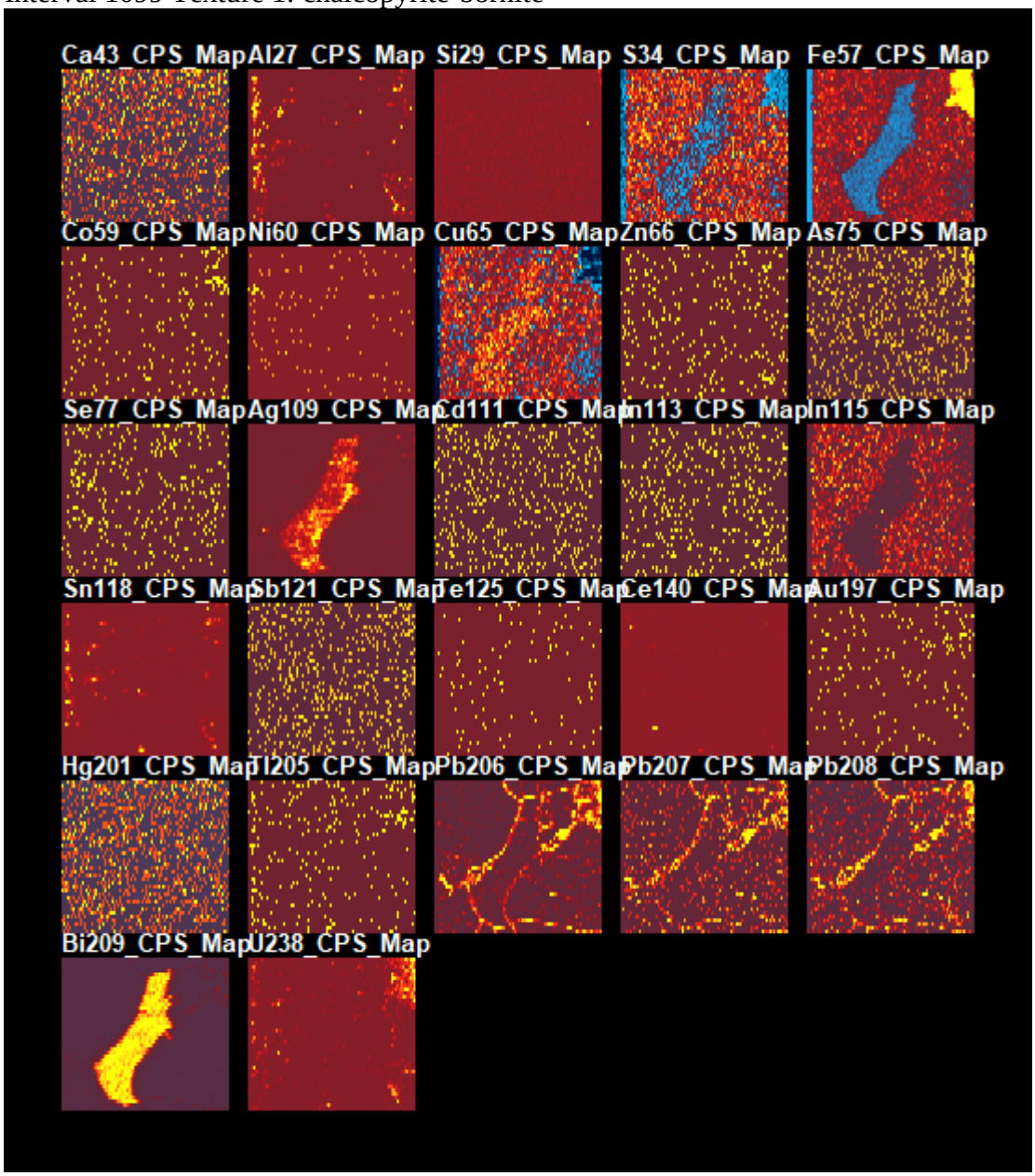

Interval 1099 Texture 2: chalcopyrite-bornite

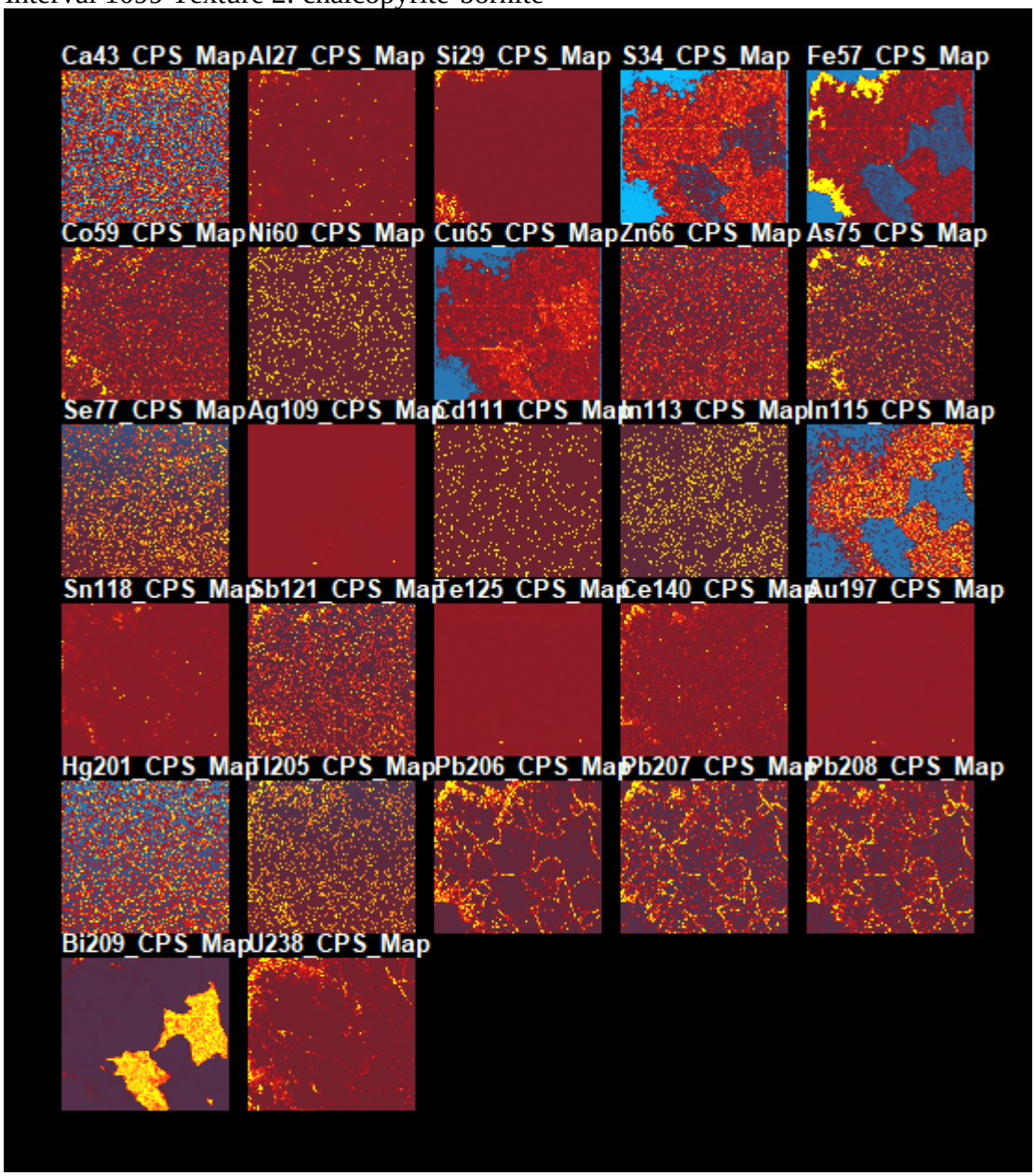

Interval 1150 Texture 1: bornite-digenite

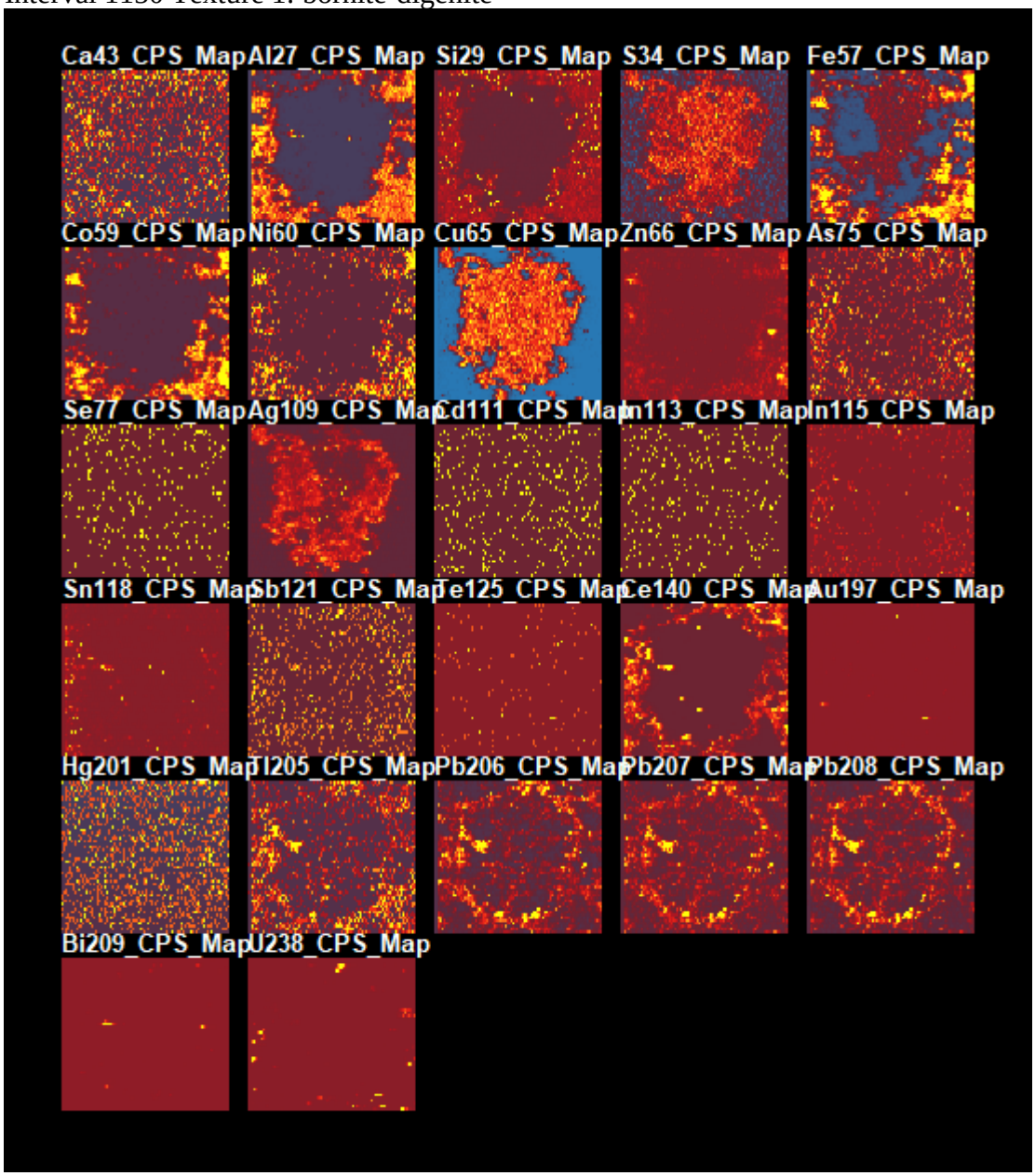

APPENDIX B: LASER SPOT ANLAYSIS

Interval 919 Laser spot Analysis locations with texture imaged in Figure 8 demarcated.

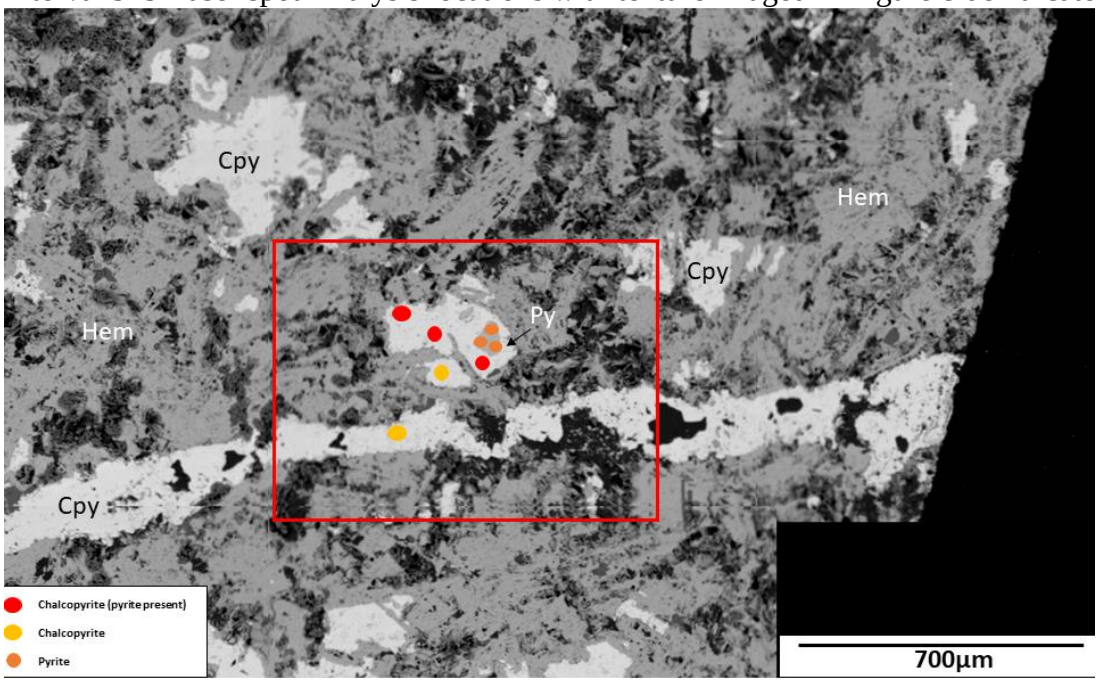

Interval 1099 laser spot analysis locations on texture image in Figure 15.

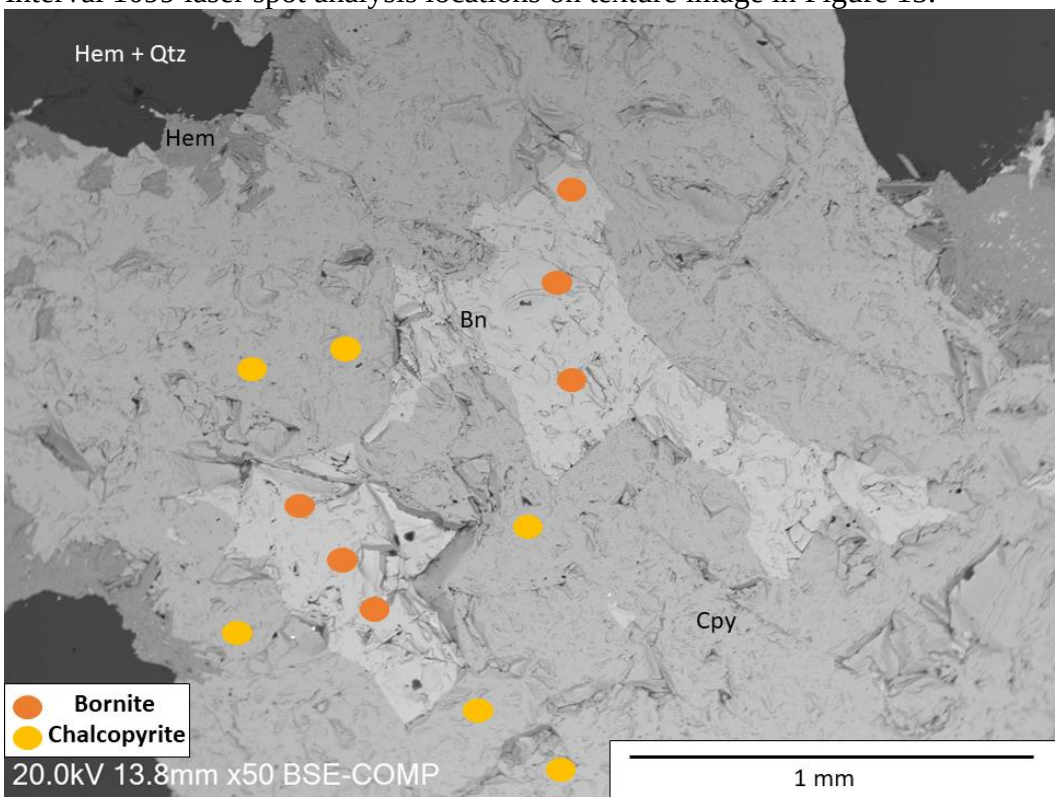

Interval 1150 laser spot analysis locations with texture imaged in Figure 17

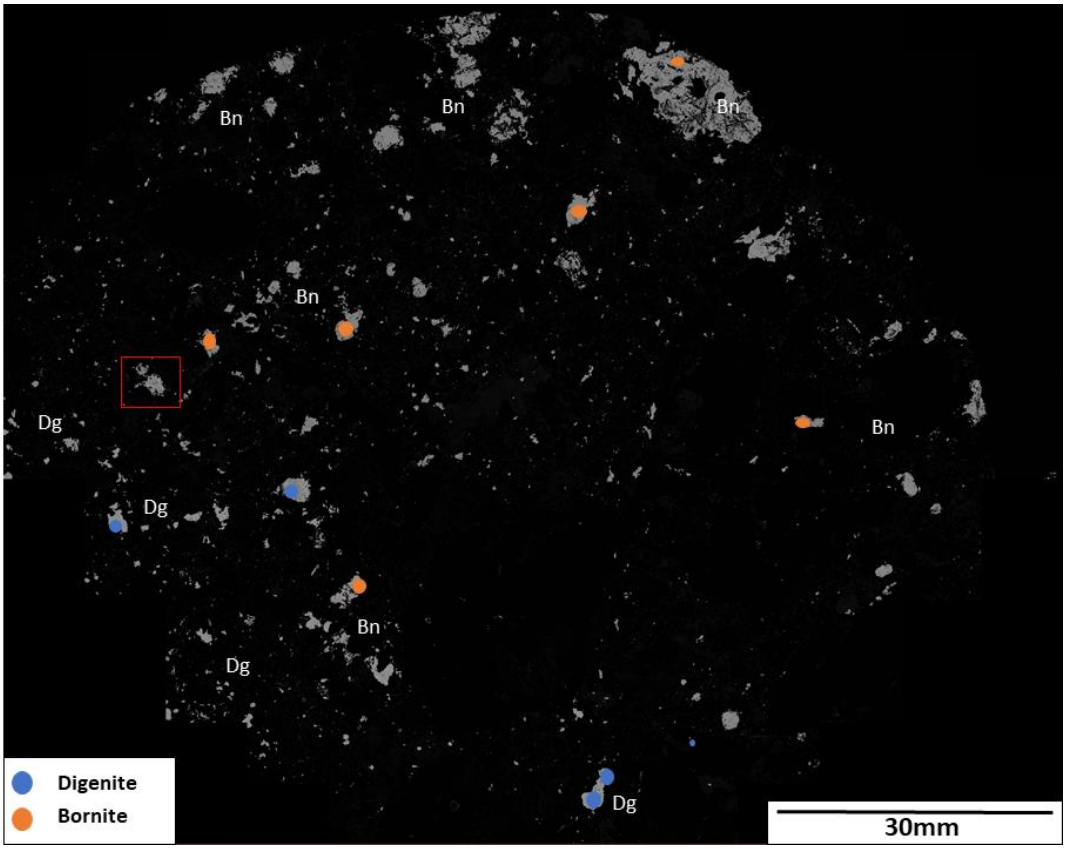
Bn
Bn
Bn
Bn
Dg
Bn
Dg
Bn
Dg
Dg
Digenite
Bornite
30mm